M 2020

U.PORTO
FEUP FACULDADE DE ENGENHARIA
UNIVERSIDADE DO PORTO

# STUDY OF AN ADSORPTIVE REACTOR FOR $CO_2$ METHANATION

**BÁRBARA JOÃO DOS SANTOS LIMA CARNEIRO MARTINS**

DISSERTAÇÃO DE MESTRADO APRESENTADA
À FACULDADE DE ENGENHARIA DA UNIVERSIDADE DO PORTO EM
ENGENHARIA QUÍMICA

Integrated Master in Chemical Engineering

# *Study of an adsorptive reactor for $CO_2$ methanation*

## Master's Thesis

by

**Bárbara João dos Santos Lima Carneiro Martins**

**Developed within the course of Dissertation**

held in

LEPABE – Laboratory for Process Engineering, Environment, Biotechnology and Energy


Supervisors:

**Doctor Carlos Eduardo Geraldes de Vasconcelos Miguel**

**Professor Luís Miguel Palma Madeira**



**July 2020**

# Acknowledgements

First of all, I would like to thank my supervisors, Doctor Carlos Miguel and Professor Luís Miguel Madeira for all the dedication and for everything they taught me throughout this dissertation.

To my colleagues from LEPABE, especially to researcher Joana Martins and to PhD student Ana Catarina Faria for all the help that contributed to making this thesis possible.

I am grateful to the teachers, laboratory technicians and all those who were part of my academic path, teaching and motivating me to always do better. Especial thanks to Engineer Luís Carlos for showing me how to “drill walls” to overcome obstacles.

To all my friends: who have lived this journey with me and with whom I keep some of the best memories of the past five years; and those who have been with me my whole life, particularly to Raquel for the most special unconditional friendship.

Also, I would like to leave a thank word to Ana Alves, the one who best understands me and is always there reminding me that “if it was easy, it would not be funny".

Finally, my sincere thanks to my family, especially to my parents for all the support and opportunities and to my brother for being an example to follow.

This work was financially supported by:

- Base Funding - UIDB/00511/2020 of the Laboratory for Process Engineering, Environment, Biotechnology and Energy – LEPABE - funded by national funds through the FCT/MCTES (PIDDAC);

- Project POCI-01-0145-FEDER-030277, funded by FEDER funds through COMPETE2020 – Programa Operacional Competitividade e Internacionalização (POCI) and by national funds (PIDDAC) through FCT/MCTES.





# Abstract

Climate change due to the greenhouse effect is, nowadays, one of the most concerning environmental issues. The use of renewable resources and the development of technologies of renewable energy production have been promoting the decarbonisation of the economy and the fulfilment of the United Nations Sustainable Development Goals. However, the evolution of these technologies has led to an excess of produced renewable energy and consequently to the need to find strategies for its use or storage. Thus, the Power-to-Gas (PtG) process appears allowing the transformation of energy from renewable sources into green hydrogen from water electrolysis. The focus of this dissertation is on the exploration of this concept combined with the biogas upgrade by methanation of the $CO_2$ present in it. Due to its high methane content, the equilibrium of the Sabatier reaction from biogas is limited. Thus, this dissertation proposes the use of a sorption-enhanced reactor (SER) where simultaneously occur both the *in-situ* water (another reaction product) removal and the biogas upgrade by methanation, overpassing the chemical equilibrium limitations and improving the purity in methane.

Initially, and upon validation with literature data, a traditional reactor was simulated at different conditions of temperature, pressure, space velocity and composition of the feed, allowing to study the influence of each parameter in the $CO_2$ conversion. Regarding the feed composition, besides studying the effect of the $H_2/CO_2$ ratio (reactants of the Sabatier reaction), several $CH_4/CO_2$ ratios, typical of biogas from biomass with different origins, were also considered. Higher $CO_2$ conversions were found for lower values of space velocity and $CH_4/CO_2$ ratio and for higher values of pressure, temperature and $H_2/CO_2$ ratio.

The concept of adsorptive reactor applied to methanation was illustrated based on experimental results obtained for a feed that contained only methanation reactants ($CO_2$ and $H_2$) and inert ($N_2$). The main advantage is related to the total conversion of $CO_2$ (at least until the breakthrough time), in the case of SER, in contrast to the 28 % conversion estimated for the traditional reactor under the same conditions.

To choose the most promising adsorbent to be applied in future work, a study based on data from the literature on different zeolites is presented. This analysis allowed to evaluate the water adsorption capacity of each material as well as water ideal selectivity regarding the other species involved in the process; it was found that, in general, these materials have high selectivity. Furthermore, among the studied zeolites, 13X BFK is the one that shows the greatest water adsorption capacity, making it ideal for this application.

**Keywords:** Sorption-enhanced reactor, $CO_2$ methanation; Power-to-Gas; biogas; zeolites.

# Resumo

As alterações climáticas como consequência do efeito de estufa são uma das maiores preocupações ambientais da atualidade. O uso de recursos renováveis e o desenvolvimento de tecnologias de produção de energia renovável têm assumido um papel crucial na promoção da descarbonização da economia e do cumprimento dos Objetivos de Desenvolvimento Sustentável das Nações Unidas. Contudo, a evolução destas tecnologias tem provocado um excesso de energia renovável produzida, levando à necessidade de encontrar estratégias para a sua utilização ou armazenamento. Surge, assim, o processo *Power-to-Gas* (PtG) que permite a transformação da energia proveniente de fontes renováveis em hidrogénio verde a partir da eletrólise da água. O foco desta dissertação prende-se na exploração deste conceito aliado ao *upgrade* do biogás através da metanação do $CO_2$ nele presente. Devido ao seu elevado teor em metano, o equilíbrio da reação de Sabatier é limitado quando se processa uma alimentação de biogás. Assim, propõe-se a utilização de um reator adsortivo (SER) onde ocorre, simultaneamente, a remoção *in-situ* de água (outro produto da reação) e o *upgrade* do biogás por metanação, colmatando as limitações ao nível do equilíbrio químico e aumentando a pureza em metano.

Inicialmente, e após validação com dados da literatura, foi simulado um reator tradicional a diferentes condições de temperatura, pressão, velocidade-espacial e composição da corrente de alimentação, permitindo estudar a influência de cada um dos parâmetros na conversão de $CO_2$. A respeito da composição da alimentação, além de estudado o efeito da razão $H_2/CO_2$ (reagentes da reação de Sabatier) foram também consideradas várias razões $CH_4/CO_2$, características de biogás proveniente de diferentes tipos de biomassa. Verificaram-se maiores conversões de $CO_2$ para valores inferiores de velocidade-espacial e razão $CH_4/CO_2$ e para valores superiores de pressão, temperatura e razão $H_2/CO_2$.

O conceito de reator adsortivo aplicado à metanação foi ilustrado com base em resultados experimentais obtidos para uma alimentação que continha apenas reagentes de metanação ($CO_2$ e $H_2$) e inerte ($N_2$). Identificou-se como principal vantagem a conversão total de $CO_2$ (pelo menos até ao tempo de rotura), no caso do SER, em contraste com os 28 % de conversão estimados para o reator tradicional nas mesmas condições.

Com vista à escolha do adsorvente mais promissor a aplicar em trabalho futuro, apresenta-se um estudo baseado em dados da literatura sobre diferentes zeólitos. Esta análise avalia a capacidade de adsorção de água em cada material, assim como a seletividade ideal da água em relação às restantes espécies envolvidas no processo; constatou-se que, no geral, estes materiais apresentam elevada seletividade. Mais ainda, entre os zeólitos estudados, o 13X BFK é o que exibe maior capacidade de adsorção de água, tornando-o o ideal para esta aplicação.

**Palavras-chave:** reator adsortivo; Power-to-Gas, metanação de $CO_2$; biogás; zeólitos.

# Declaration

I hereby declare, on my word of honor, that this work is original and that all non-original contributions are indicated and due reference is given to the author and source.

Porto, 6 July 2020

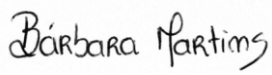

(Bárbara João dos Santos Lima Carneiro Martins)

# Index

# List of figures

# List of Tables

# Notation and Glossary

| | | |
|---|---|---|
| $C$ | molar concentration | mol·m$^{-3}$ |
| $C_{\mathrm{p}}$ | specific heat capacity | J·mol$^{-1}$·K$^{-1}$ |
| $D_{\mathrm{ax}}$ | mass axial dispersion coefficient | m$^2$·s$^{-1}$ |
| $d_{\mathrm{p}}$ | particle diameter | m |
| $E_{\mathrm{A}}$ | activation energy | kJ·mol$^{-1}$ |
| $k_0$ | pre-exponential factor of the kinetic constant | mol·s$^{-1}$·kg$^{-1}$·atm$^{-5m}$ |
| $K_0$ | pre-exponencial factor of the adsorption equilibrium constant | mol·g$^{-1}$·Pa$^{-1/n}$ |
| $K_{\mathrm{eq}}$ | equilibrium constant | |
| $K_{\mathrm{F}}$ | Freundlich adsorption constant | mol·g$^{-1}$·Pa$^{-1/n}$ |
| $K_{\mathrm{LF}}$ | Langmuir-Freundlich adsorption constant | mol·kg$^{-1}$·bar$^{-1/n}$ |
| $L$ | reactor length | m |
| $m$ | kinetic law parameter | |
| $n$ | dimensionless empirical constant | |
| $p$ | partial pressure | bar |
| $P$ | total pressure | bar |
| $Q_{\mathrm{STP}}$ | flow rate at standard temperature and pressure conditions | mL$_{\mathrm{STP}}$·min$^{-1}$ |
| $q$ | amount of adsorbed adsorbate | mol·kg$^{-1}$ |
| $q_{\mathrm{max}}$ | maximum adsorption capacity | mol·kg$^{-1}$ |
| $R_{\mathrm{g}}$ | ideal gas constant | J·mol$^{-1}$·K$^{-1}$ |
| $r$ | reactor radius | m |
| $T$ | temperature | ºC or K |
| $U$ | global coefficient for heat transfer | W·m$^{-2}$·K$^{-1}$ |
| $u_0$ | superficial velocity | m·s$^{-1}$ |
| $W$ | mass | g |
| $X$ | conversion | |
| $y$ | molar fraction | |
| $z$ | dimensionless reactor axial coordinate | |
| $\Re$ | reaction rate | mol·s$^{-1}$·kg$^{-1}$ |
| $\Delta H$ | enthalpy change | kJ·mol$^{-1}$ |
| $\beta$ | characteristic adsorption potential constant | K$^{-1}$ |
| $\delta$ | thickness | m |
| $\varepsilon$ | porosity | |
| $\boldsymbol{\zeta}$ | kinetic law parameter | atm$^{-1}$ |
| $\lambda_{\mathrm{ax}}$ | thermal axial dispersion coefficient | W·m$^{-1}$·K$^{-1}$ |
| $\mu$ | viscosity | Pa·s |
| $\rho$ | density | kg·m$^{-3}$ |
| $\vartheta$ | stoichiometric coefficient | |

### *Indexes*

| | |
|---|---|
| $\mathrm{b}$ | related to bulk |
| $\mathrm{cat}$ | related to catalyst |
| $\mathrm{ext}$ | related to the external side of the reactor |
| $f$ | related to gas mixture |
| $i$ | related to species $i$ |
| $\mathrm{in}$ | related to reactor inlet |
| $\mathrm{int}$ | related to the internal side of the reactor |
| $\mathrm{out}$ | related to reactor outlet |
| $\mathrm{p}$ | related to particle |
| $\mathrm{s}$ | related to solid |

### List of Acronyms

| | |
|---|---|
| BET | Brunauer-Emmet-Teller |
| BJH | Barrett-Joyner-Halenda |
| CAP | (Energy installed) Capacity |
| GHGs | Greenhouse Gases |
| IRENA | International Renewable Energy Agency |
| NOAA | National Oceanic and Atmospheric Administration |
| PI | Process Intensification |
| PSA | Pressure Swing Adsorption |
| PtG | Power to Gas |
| SEM | Sorption-Enhanced Methanation |
| SER | Sorption-Enhanced Reactor |
| SNG | Synthetic Natural Gas |
| STP | Standard Temperature and Pressure |
| TPR | Temperature Programmed Reduction |
| TR | Traditional Reactor |
| VPSA | Vacuum Pressure Swing Adsorption |
| XRD | X-Ray Diffraction |

# 1 Introduction

## 1.1 Motivation and relevance

Climate change due to the greenhouse effect is one of the most hotly debated issues nowadays as irreversible environmental damages are expected to be achieved[1].

Although greenhouse gases (GHGs) may occur from natural causes, in the last years, the significant increase of GHGs emission has been a result of human intervention and the evolution of industry and technology[2, 3]. Carbon dioxide is one of the most problematic GHGs and since the beginning of the industrial revolution, its concentration in the atmosphere has increased by about 47 %, counting at 414 ppm in March 2020 according to NOAA Earth System Research Laboratories[4].

Thus, promoting the use of renewable resources and improving the efficiency of renewable energy technologies is becoming increasingly important towards the decarbonization of the economy and fulfilling the United Nations Sustainable Development Goals[5].

Fig. 1.1 shows the increase of the renewable energy installed capacity (CAP) worldwide. Particularly, in Portugal, a growth of about 54 % in renewable energy capacity is verified in the indicated 10 years[6].

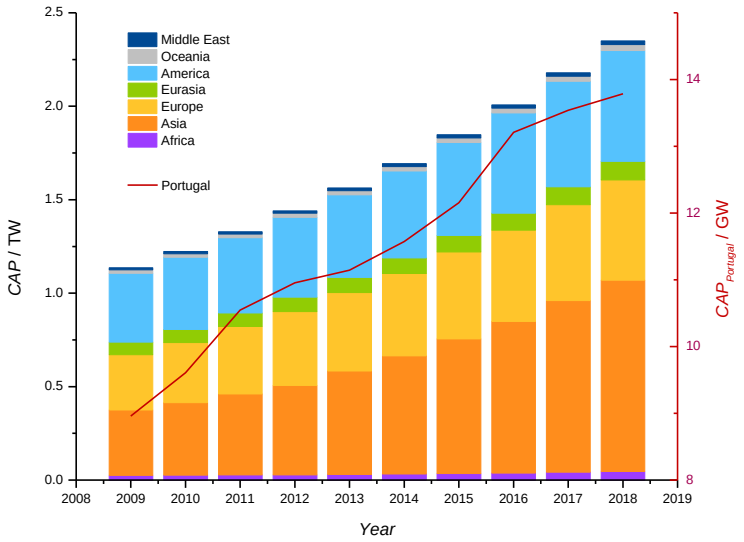


Fig. 1.1 - Renewable energy installed capacity (CAP) by region in the world (data from IRENA[6]).

Due to this increase, the generated energy can exceed the demand. To avoid wasting this renewable energy, it becomes relevant considering strategies for its use or storage technologies[7, 8].

Hence, the Power-to-Gas (PtG) concept appeared. In this approach surplus electricity from renewable sources is used for powering water electrolysers to obtain the so-called green hydrogen, besides oxygen (Eq. 1.1).

$$2H_2O \rightarrow 2H_2 + O_2 \qquad \text{Eq. 1.1}$$

Currently, some different applications for this green $H_2$ are considered. It can be blended with natural gas and directly fed to the gas grid up to a maximum between 0 % and 12 %, depending on each country grid specifications, or it can be used as vehicle fuel and for producing power and heat. Other alternative consists in converting the resulting hydrogen to produce methane, also called synthetic natural gas (SNG), through the Sabatier reaction (Eq. 1.2)[9-12].

$$CO_2 + 4H_2 \rightleftarrows CH_4 + 2H_2O \qquad \text{Eq. 1.2}$$

$$\Delta H_{(298\ K)} = -165\ \text{kJ·mol}^{-1}$$

In parallel with the Sabatier reaction, carbon monoxide production through the reverse-water gas shift reaction (Eq. 1.3) is predicted to occur as well.

$$CO_2 + H_2 \rightleftarrows CO + H_2O \qquad \text{Eq. 1.3}$$

$$\Delta H_{(298\ K)} = 41\ \text{kJ·mol}^{-1}$$

Applying the Sabatier reaction to a biogas stream is a promising possibility, as its $CO_2$ content will be converted into methane, resulting in methane-rich biogas (biomethane) to be used as bioSNG. This strategy is known as dynamic biogas upgrading[8, 13].

Biogas is a good example of a renewable energy resource which results from the breakdown of organic matter in an anaerobic environment. It is mainly composed by methane (45 - 70 %), carbon dioxide (24 - 40 %), and traces of other species (mostly $H_2S$, $O_2$, $N_2$). Biogas composition varies essentially due to the type of utilized biomass[14, 15], as shown in Table 1.1 for three types of biomass.

Table 1.1 - Typical composition of biogas depending on the type of biomass used[14].

| Component | Landfill | Sewage digester | Organic waste |
|---|---|---|---|
| $CH_4$ (%) | 45 - 62 | 58 - 65 | 60 - 70 |
| $CO_2$ (%) | 24 - 40 | 33 - 40 | 30 - 40 |
| $O_2$ (%) | 1 - 2.6 | < 1 | 1 - 5 |
| $N_2$ (%) | 1 - 17 | 1 - 8 | 1 |
| $H_2S$ (ppm) | 15 - 427 | 0 - 24 | 10 - 180 |
| $NH_3$ | Traces | Traces | Traces |
| Siloxanes | Traces | Traces | Traces |

Biogas can be used for power and heat production, but also as a vehicle fuel, as a result of the released energy from methane combustion[16].

Besides its different applications, the production of biogas by anaerobic digestion of organic wastes, along with decreasing the need for fossil fuel production, allows reducing the world's GHGs emissions by approximately 10 - 13 % of current emissions, according to The World Biogas Association[17].

Currently, Vacuum Pressure Swing Adsorption (VPSA) is one of the most mature technologies available to produce biomethane from the biogas upgrading[18]. Fig. 1.2 shows the process flow diagram of a VPSA unit for biogas upgrading.

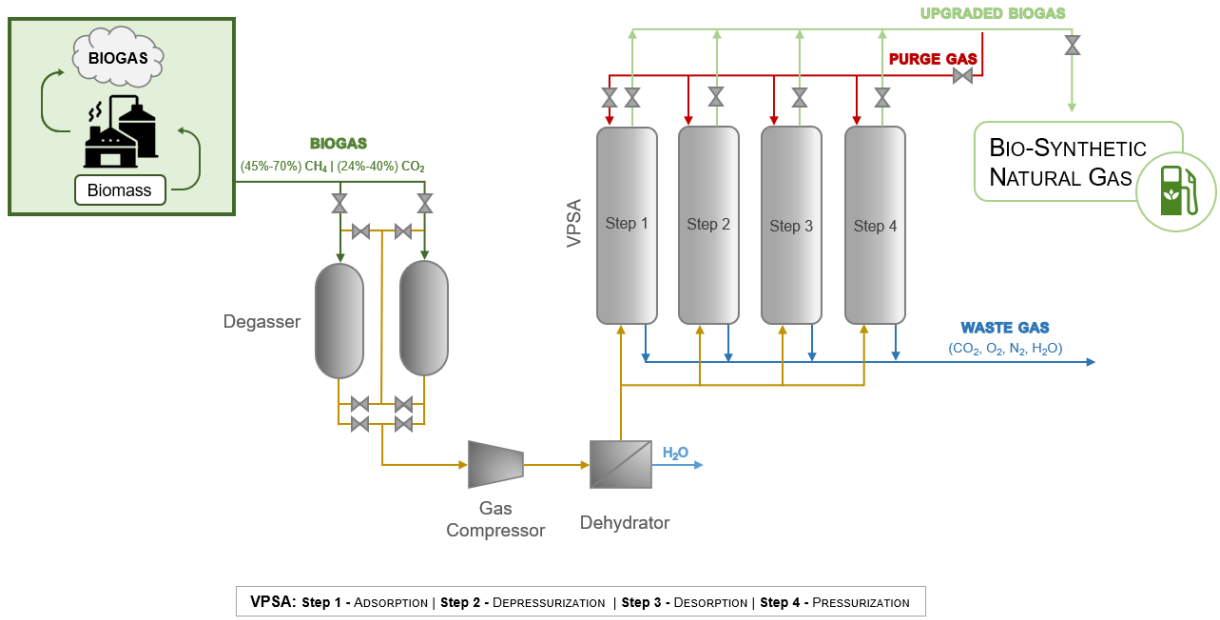


Fig. 1.2 - Process flow diagram of a VPSA unit for biogas upgrading based on the Methagen unit from Sysadvance[19].

VPSA technology requires raw biogas pre-conditioning to remove $H_2S$, $H_2O$ and siloxanes and uses porous adsorbents with high affinity for $CO_2$ for $CO_2/CH_4$ separation (typically zeolites or activated carbon) allowing to achieve high methane recoveries (up to 99.96 %) and purities (up to 99 %)[19]. The main drawback is related to the release of a $CO_2$-rich waste stream.

Thus, this work aims studying a sorption-enhanced reactor (SER) for simultaneous biogas upgrading and improved methane productivity, allowing the $CO_2$ recovery from its conversion into methane, instead of just separating and releasing it as with VPSA. The SER concept features the *in-situ* removal of steam from the reaction medium by means of a sorbent to shift the Sabatier reaction equilibrium towards the forward direction (*cf.* Eq. 1.2). This is particularly relevant since biogas contains a considerable amount of methane that limits $CO_2$ methanation.

Fig. 1.3 illustrates the proposed cyclic sorption-reaction process required for continuous operation using two sorption reactors: while one of them is producing in sorption-enhanced reaction mode,

the other is in the sorbent regeneration mode. In other words, this unit runs in a cyclic mode, like a PSA/VPSA, but with the aim of transforming $CO_2$ (which is not a waste anymore) into highly pure $CH_4$.

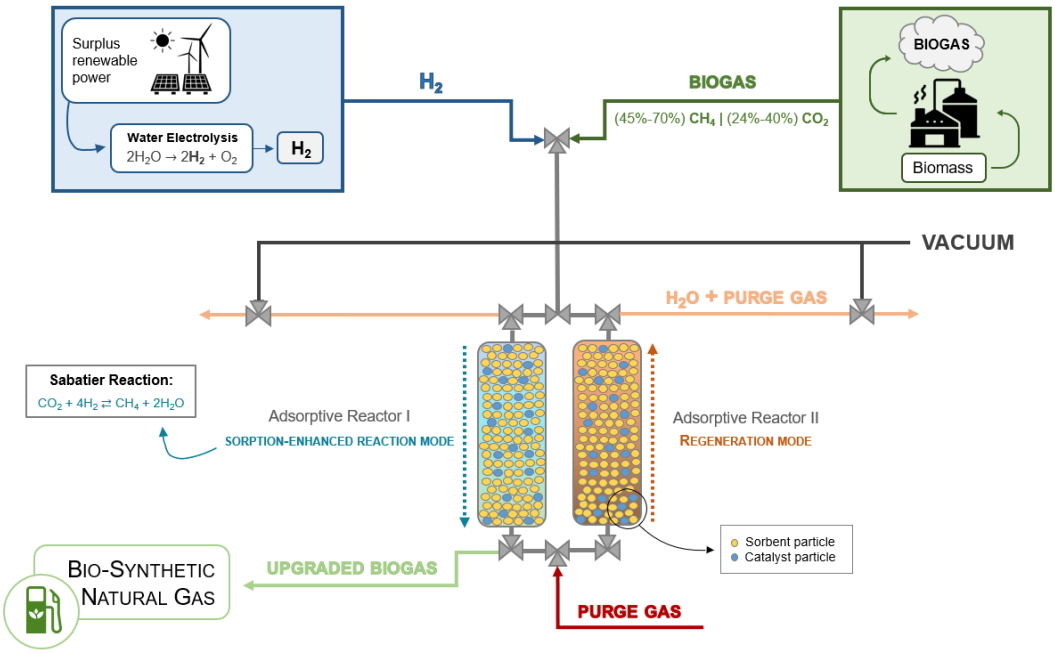


Fig. 1.3 - Sorption-enhanced reactor applied to biogas upgrading.

## 1.2 Work contribution

The main objective of this work was to compare the performance obtained with the hybrid concept of adsorptive reactor (i.e. that combines the methanation reaction with the *in-situ* adsorption of steam produced by the reaction) with a conventional fixed-bed methanation reactor for biogas upgrading. To this purpose, the following methodology has been adopted:

1 – Simulation of a conventional fixed-bed reactor to define the baseline for comparison between both reactors;

2 – Preliminary analysis of experimental results obtained with a SER packed with commercial materials (a methanation catalyst and a water-selective zeolite-based sorbent);

3 – Identification of the best water-selective adsorbent candidates through a literature review for applying in future work.

This work also envisages contributing for the following United Nations Sustainable Development Goals[5]:

- Goal 7: Affordable and Clean Energy;
- Goal 13: Climate Action.

## 1.3 Outline

The present work is divided in five chapters.

Chapter 1 addresses current environmental problems, focusing on the relevance of using renewable energy resources such as biogas. The aim of this dissertation - biogas upgrading with a sorption-enhanced reactor - as well as the adopted methodology are also described in this chapter.

Chapter 2 introduces a brief description of the process intensification concept and the principle of operation of multifunctional reactors, namely the sorption-enhanced addressed herein. Materials used in different studies are also identified/compared and the main results/conclusions reviewed.

Chapter 3 describes the materials used and the methods considered in this work. The experimental setup and procedures are presented, as well as the mathematical model proposed for the fixed bed reactor (packed with catalyst only).

Chapter 4 presents and discusses the results, starting with a parametric study based on simulation of a traditional fixed bed reactor. Afterwards, the benefits of using a sorption-enhanced reactor for $CO_2$ methanation is illustrated. Finally, an analysis on water-selective adsorbents materials is presented.

Chapter 5 presents the main conclusions of this work.

Chapter 6 provides an assessment of the developed work and suggestions for future work.

# 2 State of the art

## 2.1 Process intensification with multifunctional reactors

The process intensification (PI) concept regarding to methanation is the focus of this work. PI consists in reducing the number of chemical process units in a chemical plant, ensuring that production goals are still achieved[20]. Multifunctional reactors are innovative equipment that simultaneously perform chemical reaction and separation processes[20, 21]. These units allow, among other possibilities, removing one of the products from the reaction zone, shifting the equilibrium towards the desired reaction products according to Le Chatelier's principle and, consequently, enhancing equilibrium-limited conversions.

To carry out gas phase reactions, units such as membrane reactors and sorptive reactors can be considered[22-25]. A scheme of a membrane reactor for such a purpose is illustrated in Fig. 2.1. For molecular sieve porous membranes, for instance, the selectivity depends on the pore diameter, since only species that are smaller than the pore diameter will pass through it. Once they pass the membrane, they leave the reactor through the permeate stream[26], allowing to shift forward the desired reaction. In some configurations, the membrane itself can have a catalytic property, i.e., the material of the inner cylinder can be coated with a catalyst or even be catalytic-based[26]. Some examples of applications where membrane reactors have been considered include $H_2$ production/purification processes[25, 27, 28] and methanol production[29-31].

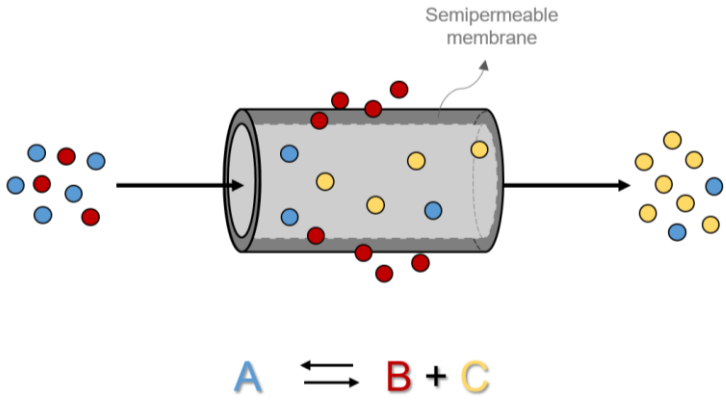


Fig. 2.1 - Scheme of a tubular membrane reactor illustrating the shift of a reversible reaction.

Sorptive reactors focused in this work can contain a mixture of a catalyst and a sorbent (Fig. 2.2 a), or alternating layers of sorbent and catalyst (Fig. 2.2 b) or even a unique kind of material with both functionalities - sorption catalyst - (Fig. 2.2 c)[22, 32]. The latter has some advantages since promotes greater proximity between adsorbent sites and catalytically active sites, reducing mass (and heat) transport limitations, and makes packing the unit easier[33].

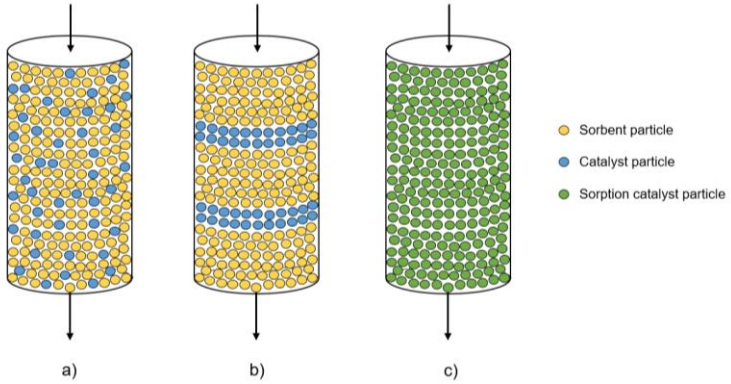


Fig. 2.2 - Scheme of different sorptive reactors: a) mixed bed, b) layered bed and c) sorption catalyst material bed.

The sorbent (or the sorptive component of the sorption catalyst) captures one of the reaction products, eliminating it from the reaction sites, shifting the equilibrium forward and improving the reaction kinetics. However, the sorption-enhancement effect becomes less effective as the sorbent saturates. At the saturation point, the shift effect no longer occurs and the reactor starts behaving as a conventional fixed-bed reactor; so, at that point, the sorbent needs to be regenerated for enhanced performance[22, 32] (e.g. by pressure or temperature swing[34]). Hence, for continuous operation, a cyclic sorption-reaction process must be implemented, using at least two sorption reactors: while one of them is producing in the sorption-enhanced reaction mode, the other is in the reactive regeneration mode[35]. For continuous operation using two units, it would be preferable if the sorbent saturation time was equivalent to the sorbent regeneration time. However, the regeneration step is, frequently, slower and the time-limiting step, thus defining the process cycle time[33].

An important and limiting issue of this kind of reactors is finding compatible catalysts and sorbents, since they must be used in the same operating conditions[32].

These systems may have some advantages, namely the reduction of investment and operating costs, the increase of productivity and selectivity and even the decrease of greenhouse gas emissions[20, 21]. Typical drawbacks include increased operation complexity and stringent process control requirements. Some applications where sorptive reactors have been considered include $H_2$ production/purification (e.g. steam reforming and water gas shift reactions)[24, 36, 37] and $CO_2$ capture and conversion[35, 38]. Based on the scope of the present work, the use of sorptive reactors for steam separation enhanced methanation will be specifically addressed in the following sections by reviewing the studies available in literature.

## 2.2 Steam separation enhanced reactors

Table 2.1 lists the main studies found in literature covering the use of steam separation enhanced reactors, the operating conditions, materials and major conclusions.

Table 2.1 - Review of sorption enhanced reactor studies based on steam separation for the Sabatier reaction [a)]: operating conditions, materials and main conclusions.

| Reference | Operating conditions | Catalyst | Water sorbent | Conclusions |
|---|---|---|---|---|
| [23] [a)] | $T$ = (200 - 330) ºC<br>$P$ = 1 atm | Not Specified | Zeolite 3A | • Under operating conditions, the zeolite 3A is suitable in what concerns to water sorption capacity. |
| [32] | $T$ = (320 - 500) ºC<br>$P$ = 1 atm | Ni | Zeolite 5A | • Sorption enhanced methanation (SEM) requires alternating methanation/drying steps, being water diffusion rate-limiting for both;<br>• In SEM, milder operating conditions are verified when compared to conventional methanation;<br>• Coking and thermal degradation are not verified under the studied operating conditions;<br>• The pore size and the water sorption capacity must be considered for the choice of the sorbent. |
| [34] | $T$ = (250 - 350) ºC<br>$P$ = 1 atm | Ni | Zeolite 4A | • 100 % conversion of $H_2$ to SNG was achieved, matching the specifications for injection in natural gas grid;<br>• Operating at low pressure leads to significant energy savings;<br>• Bifunctional materials lead to a cost effective SNG upgrading method;<br>• Energy integration can be attained by harnessing heat released by the methanation reaction. |

| | | | | |
|---|---|---|---|---|
| [39] | $T$ = (100 - 230) ºC<br>$P$ = 1.2 bar<br>$Q_{H_2}/Q_{CO_2}$ = 8 | Ni | Zeolite 5A | • The catalytic activity for methanation of $CO_2$ is higher with the sorption catalyst;<br>• Water sorption leads to a reaction yield of 100 %;<br>• Ni particles do not block the pores, remaining the zeolite structure unchanged;<br>• CO coverage grows with decreasing sorbent sorption capacity to water;<br>• The obtained sorption catalyst is appropriated to be used in biogas upgrading;<br>• Sorption enhancement is applicable to other chemical reactions. |
| [40] | $T$ = 300 ºC<br>$P$ < 1 atm | Ni | Zeolite 13X<br>Zeolite 5A | • Compared to 5Ni/5A, 5Ni/13X exhibits larger pores and, consequently, more efficient catalyst regeneration;<br>• When compared to 5Ni/5A, 5Ni/13X shows higher operation time due to its higher water sorption capacity;<br>• The catalyst regeneration should occur in an oxidizing environment to avoid deactivation due to poisoning by coke and/or sulphur. |
| [41] | $T$ = (270 - 320) ºC | Ni | Zeolite 5A | • A $CO_2$ conversion of 100 % and a high selectivity to $CH_4$ were achieved;<br>• To save energy, regeneration step should occur at the reaction temperature and may take advantage of the heat released by Sabatier reaction;<br>• The optimal temperature depends not only on the heat of water adsorption in the zeolite, but also on the catalytic activity. |

[a] Reference [23] refers to Claus reaction, unlike the others that are related to Sabatier reaction.

Several issues influencing the results obtained in these studies such as the materials employed, the influence of temperature, the sorbent pore size, sorbent regeneration strategy and sorbent selectivity will be addressed in the following sub-sections.

### 2.2.1 Materials

Catalysts play an important role in improving the reaction kinetics to achieve a favourable reaction rate at milder operating conditions.

Focusing on methanation, as it is extremely exothermic, high conversions of $CO_2$ and $H_2$ are expected, especially at low temperature. Nevertheless, this is not effectively verified because of the kinetic limitations of the reaction[39]. In order to overpass this obstacle, catalysts can be used, decreasing the activation energy and promoting a reasonable reaction rate[42]. Therefore, in what concerns to catalyst properties, high activity and high methane selectivity are required[39].

For this reaction, several studies have been performed mostly with nickel-based catalysts due to their good activity, availability and lower price when compared to noble metal-based catalysts(e.g. [32, 34, 35, 39-41]). However, some disadvantages of this kind of catalysts are described in the literature. For instance, to achieve a satisfactory carbon dioxide conversion, a high activation temperature (above 350 ºC) is required which can result in instability and reduced catalyst lifetime[43, 44]. Moreover, Delmelle *et al*.[32, 40] concluded that nickel-based catalyst regeneration must take place in an oxidizing environment as the poisoning is less likely to occur, preventing catalyst deactivation.

Noble metals (such as Ru, Rh, Pd, Ag…) supported on $Al_2O_3$, $TiO_2$, $CeO_2$ or $SiO_2$ have been preferred as they are more effective than Ni-based catalysts, i.e., they allow that a higher yield to methane is achieved at a lower temperature[44, 45]. Falbo *et al*.[44] also reported that noble metals are less susceptible to sulphur poisoning, carbon deposition or carbides formation, exhibiting more stability and tolerance to degradation. Among all the noble metals, ruthenium (Ru) is the one with the greatest activity, since a very low metal composition (e.g. 0.5 wt.% $Ru/Al_2O_3$) guarantees high $CH_4$ selectivity (> 99 %)[44].

The choice of the sorbent is also determinant for this process and, according to Delmelle *et al*.[32], the main characteristics that must be considered are the pore size and the water sorption capacity at the catalyst operation temperature. Besides, sorption kinetics must also be considered, especially if the selectivity between the species involved is low.

Among the several types of water adsorbents available, including silica gel, activated alumina, activated carbon and zeolites, this work focuses on the latter which presents advantages such as high sorption capacities and strong hydrophilicity[46, 47].

Zeolites are porous crystalline aluminosilicates, referred to as molecular sieves, that are commonly used as sorbents in the form of pellets or beads. Hydrogen purification, $CO_2$ sequestration and biogas upgrade are some examples of adsorption-based separation processes in which zeolites have been utilized[48].

Literature reports studies where zeolites were used to evaluate the effect of sorption of water as an undesired product, not only in the Sabatier[32, 34, 39-41] but also in the Claus reaction[23], which is applied to sulphur recovery from the reaction between hydrogen sulphide ($H_2S$) and sulphur dioxide ($SO_2$). The main conclusions shown in Table 2.1 are discussed below.

Elsner *et al.*[23] used zeolite 3A as water sorbent and determined that it is a suitable adsorbent to improve the $H_2S$ conversion through Claus reaction. Besides, at a range of temperature between 200 ºC and 330 ºC, zeolite 3A has been shown to have a relatively high adsorption capacity for water[23].

Regarding Sabatier reaction, several authors[32, 34, 39-41] verified greater conversion of $CO_2$ as well as greater selectivity to methane when steam sorption is applied simultaneously.

It was verified by Borgschulte *et al*.[39] that, while the zeolite is not saturated (up to approximately 750 s in Fig. 2.3 – so called breakthrough time), there is no significant amount of water, CO and $CO_2$ leaving the reactor, producing practically pure methane.

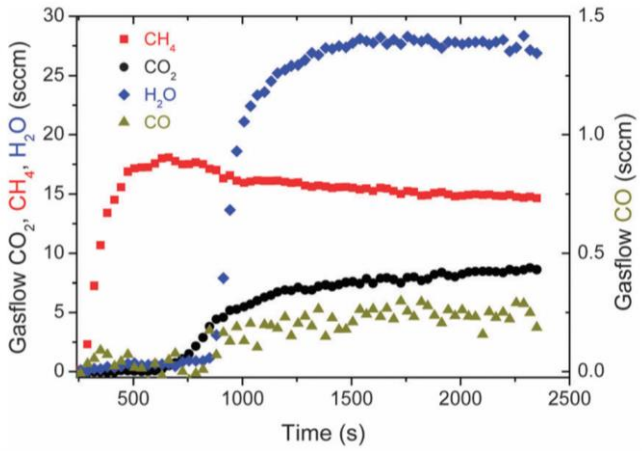


Fig. 2.3 - Time evolution of the gas composition at the outlet of the reactor at $T = 170\ °C$. Borgschulte, A., N. Gallandat, B. Probst, R. Suter, E. Callini, D. Ferri, Y. Arroyo, R. Erni, H. Geerlings, and A. Züttel, *Sorption enhanced $CO_2$ methanation.* Physical Chemistry Chemical Physics, 2013. **15**(24): p. 9620-9625. Published by the PCCP Owner Societies.

When the adsorbent is saturated, the flow rates at the outlet of the reactor correspond to those of a conventional reactor, that is, a reactor without adsorbent for water. These values can be read in Fig. 2.3 at the represented steady-state level after the breakthrough. Thus, in a conventional reactor, there is a higher flow rate of $CO_2$ at the outlet, which corresponds to a lower conversion of this reagent and, consequently, to a lower production of methane. Unlike what happens in the adsorptive reactor before the breakthrough, water and CO are released in the outlet stream.

### 2.2.2 The influence of temperature

Considering sorption enhanced methanation, Stéphane Walspurger *et al*.[34] evaluated the influence of the operating temperature in water sorption capacity. Observing Table 2.2 it is notable that as the temperature increases, the $H_2O$ breakthrough time decreases as a result of decreased water sorption capacity[34] - the sorption capacity decayed 29.6 % when increasing the temperature from 250 ºC to 350 ºC (*cf.* Table 2.2).

Table 2.2 - The influence of operating temperature in water breakthrough time for $p_{H_2O} = 0.039\ bar$[34].

| Operating temperature (ºC) | $H_2O$ breakthrough time (min) | Water sorption capacity (mmol/g) |
|---|---|---|
| 250 | 16.3 | 1.52 |
| 300 | 14.0 | 1.31 |
| 350 | 11.3 | 1.07 |

However, lowering the temperature is not convenient because the catalyst is less active and release of unreacted $CO_2$[41] may occur.

### 2.2.3 The influence of sorbent pore size

The pore size of the zeolite employed should be considered depending on the kinetic diameter of the compounds involved in the reaction. Regarding Sabatier reaction, Delmelle *et al*.[32, 40] referred that pore size ≥ 5 Å promotes methane production. Thus, they assessed the effectiveness of zeolite 13X (LTX) – with a pore size equal to 9 Å - and zeolite 5A (LTA) - with a pore size of 5 Å - in water sorption enhanced methanation at a mean temperature of 300 ºC. Due to larger pores size, zeolite 13X showed greater efficiency in regeneration because of the easier air and water transport[32, 40].

### 2.2.4 Milder operating conditions

When sorbent reaches the saturation point, the sorption-enhanced reactor starts behaving like a conventional methanation reactor. Andreas Borgschulte *et al*.[39] used a sorption catalyst (i.e., a dual function material) and compared the outlet concentrations of $CO_2$ and $CH_4$ at the initial point (unsaturated sorbent) and at the equilibrium (saturated sorbent). Fig. 2.4 shows that this hybrid catalyst based on Ni and zeolite 5A promotes $CO_2$ conversion at lower temperatures than it would happen with a commercial catalyst. Furthermore, this phenomenon is less evident at the extremes of the temperature range. At low temperature, the catalyst activity is not enough to promote the Sabatier reaction, leading to low $CO_2$ conversion. On the other hand, at high temperature (that corresponds to high $CO_2$ conversion), the reduced amount of $CO_2$ available in the gas phase

limits the reaction rate and the sorbent capacity is detrimentally affected, as discussed in the section 2.2.2. At intermediate conversion values, a difference of about 10 ºC between both cases (unsaturated and saturated sorbent) is visible[39].

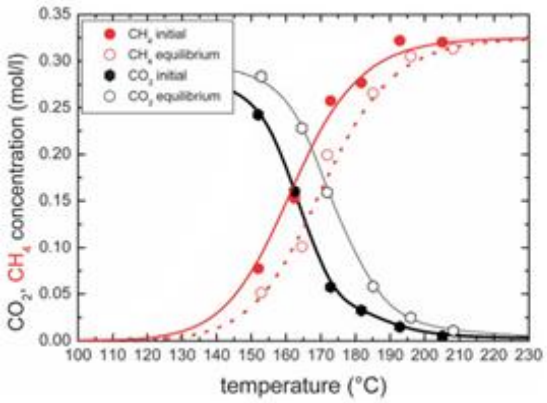


Fig. 2.4- Temperature dependence of the outlet concentrations of $CO_2$ and $CH_4$ – with (‘‘initial’’) and without (‘‘equilibrium’’) maximum sorption enhancement. Borgschulte, A., N. Gallandat, B. Probst, R. Suter, E. Callini, D. Ferri, Y. Arroyo, R. Erni, H. Geerlings, and A. Züttel, *Sorption enhanced $CO_2$ methanation.* Physical Chemistry Chemical Physics, 2013. **15**(24): p. 9620-9625. Published by the PCCP Owner Societies.

Another relevant advantage of sorption enhanced methanation (SEM) is that it allows operating under lower pressures, reducing energy consumption for compression. This has been shown in the work by Walspurger *et al.*[34] where a sorption catalyst based on Ni and zeolite 4A was used to study the SEM applied to the production of synthetic natural gas. It was shown that $H_2$ is almost completely converted using the sorption-enhanced reactor, when compared to a conventional methanation process, and the obtained outlet $H_2$ content satisfy the Netherlands gas grid specifications at a much lower pressure (*cf.* Fig. 2.5).

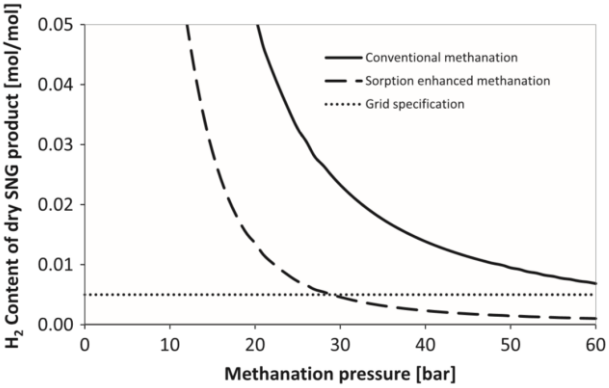


Fig. 2.5 - H2 level in SNG produced for the conventional methanation case and for the sorption enhanced methanation case. The horizontal dotted line represents the maximum amount of $H_2$ allowed in the Dutch gas grid. Reprinted from Chemical Engineering Journal, 242, Stéphane Walspurger, Gerard D. Elzinga, Jan Wilco Dijkstra, Marija Sarić,Wim G. Haije, Sorption enhanced methanation for substitute natural gas production: Experimental results and thermodynamic considerations, 379-386, Copyright (2014), with permission from Elsevier.

### 2.2.5 Sorbent regeneration

Sorbent regeneration is necessary when the sorbent reaches the saturation point for continuous operation. Regeneration can be achieved by varying temperature or pressure, with or without a purge gas. The energy requirement depends not only on operating conditions (temperature, pressure, purge gas flow rate) but also on the adsorption energy of steam on the sorbent material[34]. Pressure swing is commonly preferred over temperature swing since the latter is typically a much slower process[33].

Regarding purge gas, it was mentioned the convenience of choosing an inert such as nitrogen or helium[34]. To avoid diluting the outlet stream also $CO_2$ or $H_2$ obtained by water electrolysis could be used as purge gas. However, the selectivity of the adsorbent to these species must be considered as well as it must be ensured that $H_2$ is previously dried and that the stability of the catalyst is not affected. Still, economics of the process have to take into consideration of the gas used to regenerate the adsorbent.

It was also found that the regeneration temperature does not have to be much higher than the operating temperature[34] and some studies showed the possibility of using the heat released by the methanation reaction for water desorption, avoiding energy losses and improving the energy efficiency of the process[34, 41].

### 2.2.6 Sorbent selectivity

It must be considered the possibility of the zeolite can adsorb other species besides water, limiting the performance of the sorption enhanced reactor.

Zeolites are generally considered very effective in $CO_2$ adsorption[49]. Rute Seabra *et al*.[48, 50] studied the adsorption equilibrium of $CO_2$, $N_2$ and $CH_4$ over zeolites 4A and 13X at a temperature range between 30 ºC and 100 ºC. It was verified that zeolite 13X shows higher water sorption capacity than zeolite 4A, but both type of zeolites can adsorb all the species, being $N_2$ the less adsorbed gas and $CO_2$ the most adsorbed. It has also been reported that the sorption capacity of binder-containing zeolites is usually 18 - 20 wt.% lower than that of binder-free zeolite[50].

At a temperature range of (200 - 300) ºC and a $p_{CO_2}$ of 0.025 bar, Walspurger *et al*.[34] reported that although the sorption capacity of $CO_2$ over zeolite 4A is practically negligible, its presence reduces the water adsorption capacity by about 15 - 20 %.

Zhu *et al.* studied zeolite 4A and showed that temperature could influence the selectivity for $H_2O$ over other gases of interest. In a temperature range of 27 ºC to 107 ºC, it was verified that selectivity for water over $H_2$ practically does not depend on temperature, whereas over CO and $CH_4$ decreases and increases with temperature, respectively[51].

Yu Wang and M. Douglas LeVan determined $CO_2$ isotherms on zeolites 5A and 13X for a temperature range of -45 ºC to 175 ºC, as well as for $H_2O$ between 0 ºC and 100 ºC[52]. The results show that the sorption capacity is greater for water than for carbon dioxide for the two zeolite types, being slightly higher for zeolite 5A.

Finally, high affinity of zeolite 3A for water was determined by Bruno Santos[53]. The small pore size of the zeolite only allows molecules with a kinetic diameter smaller than 3 Å to enter. Thus, taking into account the kinetic diameters referred in the literature ($CO_2$ - 3.3 Å; $H_2$ - 2.9 Å; $CH_4$ - 3.8 Å; $H_2O$ - 2.65 Å; CO - 3.2 Å; $N_2$ - 3.6 Å)[54], among all the species involved in the process, water is the one that is most easily adsorbed over the zeolite 3A.

## 2.3 Steam separation enhanced reactors applied to biogas upgrading

Some technologies such as water scrubbing (with a market share of 41 %), chemical absorption (22 %), pressure swing adsorption - PSA - (21 %) and membrane separation (10 %) are widely applied to biogas upgrading[55] since they mainly consist in the removal of the contaminants present in biogas. However, there are also strategies where the $CO_2$ present in biogas is converted into methane instead of just being separated[8, 13].

According to the scope of the present work, the sorption-enhancement concept applied to biogas upgrading could bring at first sight some advantages such as:

- A single chemical process unit required for simultaneous separation and conversion of $CO_2$;
- Enhanced equilibrium conversion and product selectivity: the equilibrium is shifted towards the forward direction due to water removal, overpassing the limitation caused by the methane present in the feed, thus overcoming performance of conventional fixed-bed reactors.

Another advantage evidenced by a theoretical study[15] is the fact that *in-situ* water removal reduces the production of carbon oxides, improving the biogas quality according to the specifications for injection in the natural gas grid.

# 3 Material and methods

## 3.1 Fixed bed simulations (reactor packed with catalyst only)

For fixed bed simulations performed in this work, it was used a MATLAB® program developed at LEPABE where the *bvp4c* function was used for solving the model equations. Each simulation was performed considering 200 intervals along the reactor length.

The non-isothermal one-dimensional pseudo-homogenous plug flow model with axial dispersion was proposed for describing the steady-state reactor performance. The oven temperature and the bed porosity were considered constant while the superficial velocity varies along the reactor length. Ideal gas behaviour was assumed for all the involved species. Equations and parameters required to estimate the physical properties can be found in Appendix A.

The proposed model considered the following equations whose variables are explained in the Notation and glossary section.

- Global mass balance:

$$\frac{d\left(u_0\, C_{i_\mathrm{b}}\right)}{L\, dz} - \rho_\mathrm{b} \sum_i (\vartheta_i)\ \Re = 0 \qquad \text{Eq. 3.1}$$

- Partial mass balance for species $i$:

$$\frac{D_\mathrm{ax}\ \varepsilon_\mathrm{b}}{L^2}\ \frac{d^2 C_{i_\mathrm{b}}}{dz^2} - \frac{d\left(u_0\, C_{i_\mathrm{b}}\right)}{L\, dz} + \rho_\mathrm{b}\ (\vartheta_i\ \Re) = 0 \qquad \text{Eq. 3.2}$$

- Energy balance:

$$\frac{\lambda_\mathrm{ax}}{L^2}\ \frac{d^2 T_\mathrm{b}}{dz^2} - \frac{u_0\ \rho_\mathrm{f}}{L}\ \frac{d\left(T_\mathrm{b}\ C_{\mathrm{p,f}}\right)}{dz} + \rho_\mathrm{b}\ (-\Delta H)\ \Re - \frac{2\,\pi\, r_\mathrm{int}}{\pi\, {r_\mathrm{int}}^2}\ U\ (T_\mathrm{b} - T_\mathrm{oven})\ = 0 \qquad \text{Eq. 3.3}$$

- Momentum balance (Ergun Equation):

$$\frac{dP}{dz} = -L\left(150\ \frac{(1-\varepsilon_\mathrm{b})^2\ \mu_\mathrm{f}}{{\varepsilon_\mathrm{b}}^3\ {d_\mathrm{p}}^2} u_0 + 1.75\ \frac{(1-\varepsilon_\mathrm{b})\ \rho_\mathrm{f}}{{\varepsilon_\mathrm{b}}^3\ d_\mathrm{p}}\ {u_0}^2\right) \qquad \text{Eq. 3.4}$$

- Boundary conditions:

$z = 0$ :

$$\frac{dC_{i_b}}{dz} = -\frac{u_0\, L}{\varepsilon_b\, D_{ax}} \left(C_{i_b}{}^{in} - C_{i_b}\right) \quad \text{Eq. 3.5}$$

$$\frac{dT_b}{dz} = -\frac{\rho_f\, C_{p,f}\, u_0\, L}{\lambda_{ax}} \left(T_b{}^{in} - T_b\right) \quad \text{Eq. 3.6}$$

$$u_0^{in} = u_0 \quad \text{Eq. 3.7}$$

$$P^{in} = P \quad \text{Eq. 3.8}$$

$z = 1$ :

$$\frac{dC_{i_b}}{dz} = 0 \quad \text{Eq. 3.9}$$

$$\frac{dT_b}{dz} = 0 \quad \text{Eq. 3.10}$$

Fig. 3.1 illustrates the considered reactor drawings.

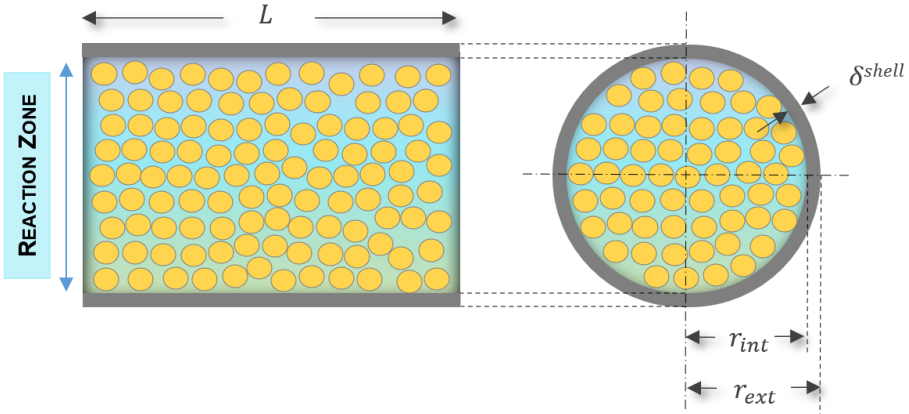


Fig. 3.1 - Longitudinal and cross-section views of the tubular packed-bed reactor.

## 3.2 Sorption enhanced $CO_2$ methanation experiment

This section describes the used material as well as the experimental setup and procedure considered for the demonstration of the sorption enhanced $CO_2$ methanation reactor.

### 3.2.1 Reactor packing material

The materials for packing the reactor column were strategically chosen and placed according to the intended objectives.

For this work, a 0.5 wt.%Ru/$Al_2O_3$ commercial catalyst from Sigma Aldrich was selected for the methanation reaction. It shows a cylindrical shape and has a characteristic length (ratio between volume and surface area) of 3.2 mm.

To demonstrate the sorption enhanced $CO_2$ methanation reactor, a bead-shaped zeolite 4AK (pore size of 4 Å) from CWK with a particle size of 1.6 - 2.5 mm was used as water sorbent.

### 3.2.2 Materials characterization

Helium pycnometry was performed to determine the true (or solid) density - $\rho_s$ - of the reactor packing material, i.e., catalyst, zeolite and glass spheres. Helium is the chosen gas since, in addition to being inert, it allows to accurately determine the volume of solid due to the small size of its atoms and the consequent ease of penetration into the pores of the sample.

A mercury porosimeter (PoreMaster 60 from Quantachrome) was used to determine the particle (or apparent) density - $\rho_p$ - of the catalyst and of the zeolite. The particle porosity ($\varepsilon_p$) was retrieved from Eq. 3.11 and the bulk density ($\rho_b$) from Eq. 3.12.

$$\varepsilon_{\mathrm{p}} = 1 - \frac{\rho_{\mathrm{p}}}{\rho_{\mathrm{s}}} \qquad \text{Eq. 3.11}$$

$$\rho_{\mathrm{b}} = (1 - \varepsilon_{\mathrm{b}})\, \rho_{\mathrm{p}} \qquad \text{Eq. 3.12}$$

Textural properties of the sample were obtained by $N_2$ physical adsorption at -196 ºC, utilizing an ASAP 2420 equipment from Micromeritics (Norcross, GA, USA). The samples were firstly degassed at 120 ºC, under vacuum, for 8 h. The BET (Brunauer-Emmet-Teller) method for a relative pressure range of (0.05 – 0.3) was chosen to calculate the specific surface area while BJH (Barrett-Joyner-Halenda) model was used to estimate pore volume, having in mind the desorption branch of the isotherm[56, 57].

X-Ray Diffraction (XRD) was performed using an X'Pert PRO MRD diffractometer (Malvern PANalytical, Malvern, UK) with Cu K-α1 radiation (wavelength of 1.5406 Å) at 45 kV and 40 mA. The XRD patterns were determined in the 2θ range of 5 - 80 º for 30 min and the metal crystallite size was obtained by the Scherrer equation[58].

Temperature programmed reduction (TPR) was performed to study the reducibility of the catalyst (sample of 50 mg) under an atmosphere with 5 % (v/v) of $H_2$ diluted in argon (total flow rate of 30 $cm^3_{STP}{\cdot}min^{-1}$). In the experiment, the temperature was gradually increased (5 $ºC{\cdot}min^{-1}$) until 850 ºC. The TPR was performed using a AMI-200 (Altamira Instruments, Pittsburgh, PA, USA) unit and $H_2$ consumption was determined using a thermal conductivity detector.

### 3.2.3 Experimental setup description

The experimental setup consists in a stainless-steel reactor with a length and an internal diameter of 15.0 cm and 2.08 cm, respectively, placed inside a tubular oven (model Split from Termolab, Fornos Eléctricos, Lda.). The available gases were fed to the reactor through mass flow controllers (model F201 from Bronkhorst-High Tech). Hydrogen ($H_2$), carbon dioxide ($CO_2$) and nitrogen ($N_2$) from Air Liquide had a purity of 99.9995 %, 99.998 %, 99.9995 % respectively. To measure the pressure, it was used a pressure transducer (model PMP 4010 from Druck) placed before the reactor. The temperature inside the reactor was measured at four different positions along the reactor (20 %, 40 %, 60 % and 80 % of the length of the reactor) with four type-K thermocouples. The flow rate of the resulting stream was quantified using a mass flow meter (model F101 from Bronkhorst-High Tech). An online gas analyser (model 4210 from Servomex) was used to measure the outlet $CO_2$ concentration.

Fig. 3.2 shows a schematic diagram of the experimental setup utilized in this work.

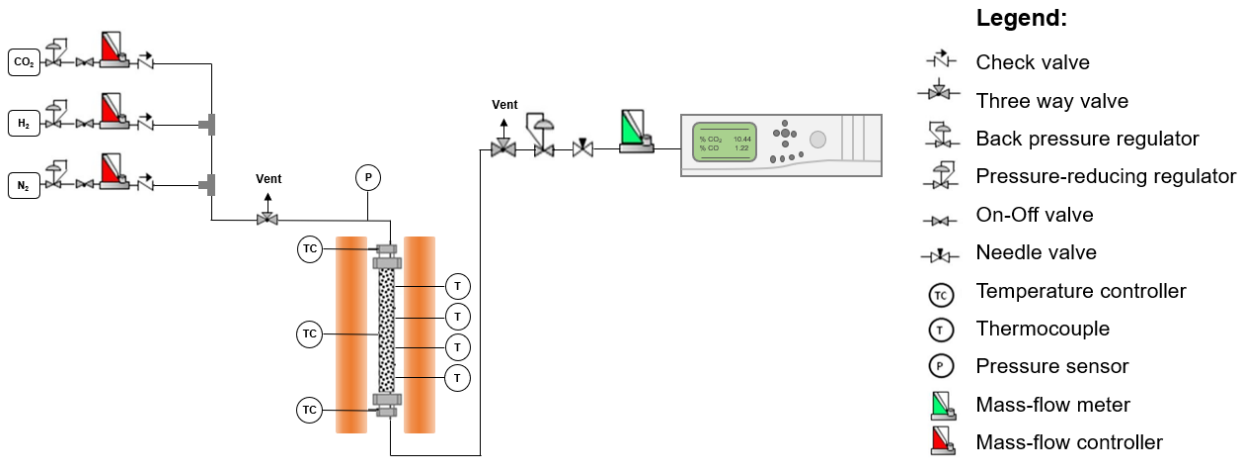


Fig. 3.2 - Schematic diagram of the experimental setup used for the sorption-enhanced $CO_2$ methanation.

### 3.2.4 Experimental procedure

The tubular reactor was packed with a mixture of the considered Ru-based catalyst (10.7 g) and zeolite 4AK (38.7 g). The top of the reactor was packed with 1.28 g layer of catalyst to avoid packing with unused sorbent. The remainder catalyst was uniformly mixed with the zeolite to fill the rest of the reactor.

The experiment was performed at 250 ºC and 1 bar. It was used a total flow rate at STP conditions of 200 $mL_{STP} \cdot min^{-1}$, corresponding to a space velocity of 18.7 $mL_{STP} \cdot min^{-1} \cdot g_{cat}^{-1}$. The feed composition consisted of 10 % of $CO_2$, 40 % of $H_2$ and 50 % of $N_2$.

Catalyst activation was performed by heating the reactor at 1 $ºC \cdot min^{-1}$ for 3 h until 250 ºC and flowing a 10 % $H_2/N_2$ feed.

# 4 Results and discussion

## 4.1 Densities of the reactor packing material

The true density ($\rho_s$) and particle density ($\rho_p$) of the reactor packing materials were determined by helium pycnometry and mercury porosimetry, respectively. The particle porosity ($\varepsilon_p$) was obtained from Eq. 3.11.

Table 4.1 - Densities and particle porosity of the reactor packing material.

| Material | $\rho_s$ (g·cm$^{-3}$) | $\rho_p$ (g·cm$^{-3}$) | $\varepsilon_p$ |
|---|---|---|---|
| Catalyst (0.5 wt.%Ru/$Al_2O_3$) | 3.17 | 1.79 | 0.435 |
| Adsorbent (Zeolite 4AK) | 2.01 | 1.43 | 0.287 |

## 4.2 Catalyst characterization

The measured BET specific area of the catalyst was 102 m$^2$/g and the pore volume 0.21 cm$^3$/g, which are in agreement with other values reported in the literature for the same catalyst (103 m$^2$/g and 0.24 cm$^3$/g, respectively)[44].

The graph of Fig. 4.1 represents the results obtained by XRD. It shows three peaks at 2θ approximately equal to 37 º, 46 º and 67 º, which correspond to the typical γ-$Al_2O_3$ structure reflections. Due to ruthenium low concentration, its reflections were not identified, only those of the catalyst support.

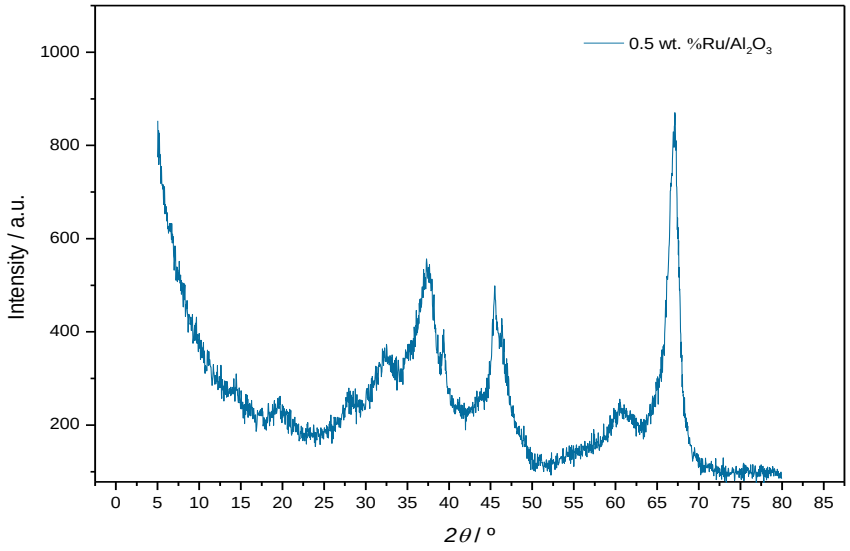


Fig. 4.1 - X-Ray Diffraction for 0.5 wt.%Ru/$Al_2O_3$.

Fig. 4.2 illustrates the TPR results. The highest $H_2$ consumption was centred at 225 ºC, what is in line with the typical reduction temperature of $RuO_2$ into $Ru^0$[59].

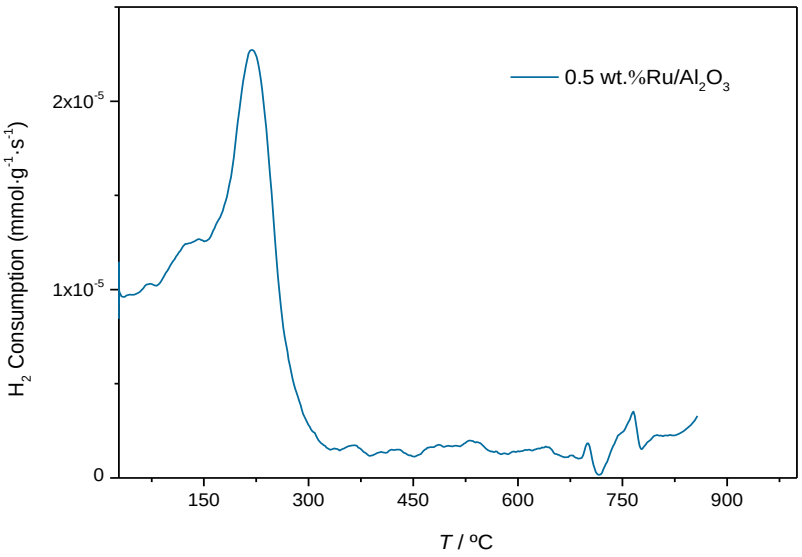


Fig. 4.2 - Temperature Programmed Reduction for 0.5 wt.%$Ru/Al_2O_3$.

## 4.3 Fixed bed simulations

For fixed bed simulations performed in this work, it was used the MATLAB® program described in section 3.1.

### 4.3.1 Validation of the kinetic model

The kinetics of the Sabatier reaction is described by Eq. 4.1[44].

$$\Re = \frac{k_0 \exp\left(-\frac{E_A}{R_g T}\right)}{1 + \zeta\, p_{H_2O}} \left( [p_{CO_2}]^m [p_{H_2}]^{4m} - \frac{[p_{CH_4}]^m [p_{H_2O}]^{2m}}{[K_{eq}(T)]^m} \right) \qquad \text{Eq. 4.1}$$

$p_i$ stands for partial pressure of species $i$, $K_{eq}$ is the equilibrium constant, $R_g$ is the ideal gas constant and $T$ represents temperature. $m$, $\alpha$, $E_A$ (activation energy), $k_0$ (pre-exponential factor of the kinetic constant) are all estimated kinetic parameters whose values are presented in Table 4.2.

Table 4.2 - Kinetic parameters estimated by Leonardo Falbo *et al*.[44].

| $k_0$ (mol·s$^{-1}$·kg$^{-1}_{cat}$·atm$^{-5m}$) | $E_A$ (kJ·mol$^{-1}$) | $m$ | $\zeta$ (atm$^{-1}$) |
|---|---|---|---|
| 95.43×10$^3$ | 75.3 | 0.152 | 0.91 |

The equilibrium constant ($K_{eq}$) is obtained from Eq. 4.2[44].

$$K_{\mathrm{eq}}(T) = \exp\left[\left(\frac{1}{1.987}\right)\left(\frac{56000}{T^2} + \frac{34633}{T} - 16.4\,ln(T) + 0.00557\,T\right) + 33.165\right] \qquad \text{Eq. 4.2}$$

To validate the developed MATLAB® code, the kinetic model from Falbo *et al*.[44] (Eq. 4.1) was implemented and the same operation conditions employed in their study were considered to check if the simulation outputs fit the experimental data obtained by those authors (*cf.* Fig. 4.3).

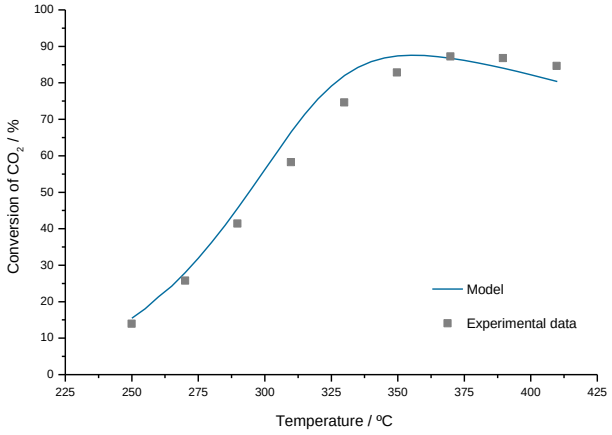


Fig. 4.3 - Validation of the kinetic and reactor model. Experimental data from Falbo *et al.*[44].

Fig. 4.3 shows that the simulation outputs fits quite well the experimental data values, in almost whole temperature range, allowing to validate the developed model.

### 4.3.2 Parametric study

Fixed bed simulations were performed to study the effect of varying operating conditions on $CO_2$ conversion. The studied parameters were the composition of the feed stream ($y_i$) (by changing the $\mathrm{CH_4/CO_2}$ and $\mathrm{H_2/CO_2}$ ratios), the pressure ($P$), the temperature ($T$) and the space velocity ($Q_{STP}/W_{cat}$). $Q_{STP}$ stands for the total flow rate ($mL_{STP}\cdot min^{-1}$) and $W_{cat}$ ($g_{cat}$) is the mass of the catalyst.

Simulation 1, whose operating conditions are presented in Table 4.3, was used as a reference for comparing with the others.

Table 4.3 - Reference simulation conditions (simulation 1).

| $P$ (bar) | $T$ (ºC) | $Q_{STP}/W_{cat}$ $\left(\frac{mL_{STP}}{min^{-1}\cdot g_{cat}{}^{-1}}\right)$ | $y_{CO_2}$ | $y_{H_2}$ | $y_{CH_4}$ | $y_{H_2O}$ | $y_{N_2}$ | $H_2/CO_2$ ratio | $CH_4/CO_2$ ratio |
|---|---|---|---|---|---|---|---|---|---|
| 1.00 | 250 | 40.0 | 0.154 | 0.615 | 0.192 | 0.000 | 0.0385 | 4.00 | 1.25 |

Table 4.4 presents the studied parameters, the considered range for each one and the respective simulations. For each simulation, all reference conditions were maintained except for the parameter under study.

Table 4.4 - Parametric study plan: parameters, considered range and respective simulations.

| Parameter | Range | Considered simulations |
|---|---|---|
| $CH_4/CO_2$ ratio | 0.00 – 2.50 | 1 - 5 |
| $H_2/CO_2$ ratio | 4.00 – 6.00 | 1, 6, 7 |
| Pressure (bar) | 1.00 – 1.50 | 1, 8 |
| Temperature (ºC) | 180 - 260 | 1, 9 - 12 |
| Space velocity ($mL_{STP} \cdot min^{-1} \cdot g_{cat}^{-1}$) | 20.0 - 100 | 1, 13 - 18 |

The packed bed porosity ($\varepsilon_b$) was set equal to 0.4 and the considered reactor had 15.0 cm length and 2.08 cm inside diameter.

It must be referred that the used kinetic model (Eq. 4.1) is only valid for temperatures between 250 ºC and 410 ºC. However, temperatures above 250 ºC are not favourable for the zeolite performance when SER is considered. For simulation purposes, it was assumed that the kinetic model would also be valid for temperatures below 250 ºC, which however should be further verified through catalytic tests in the laboratory.

In the following sections (4.3.2.1 to 4.3.2.5), the effect of the studied parameters on $CO_2$ conversion will be discussed. Table 4.5 (pp. 30-31) summarizes the operating conditions considered in each simulation and respective $CO_2$ conversion values at the outlet of the reactor ($z = 1$).

#### 4.3.2.1 Effect of $CH_4/CO_2$ ratio

The effect of the feed composition on $CO_2$ conversion was evaluated by varying the $CH_4/CO_2$ ratio (simulations 1 to 5). Simulations 1 to 4 consider typical biogas compositions from different origins; simulation 5 considers an ideal feed with only reagents from the methanation reaction (i.e., without $CH_4$ in the feed). Fig. 4.4 illustrates how the variation of $CH_4/CO_2$ ratio affects the $CO_2$ conversion along the reactor dimensionless length.

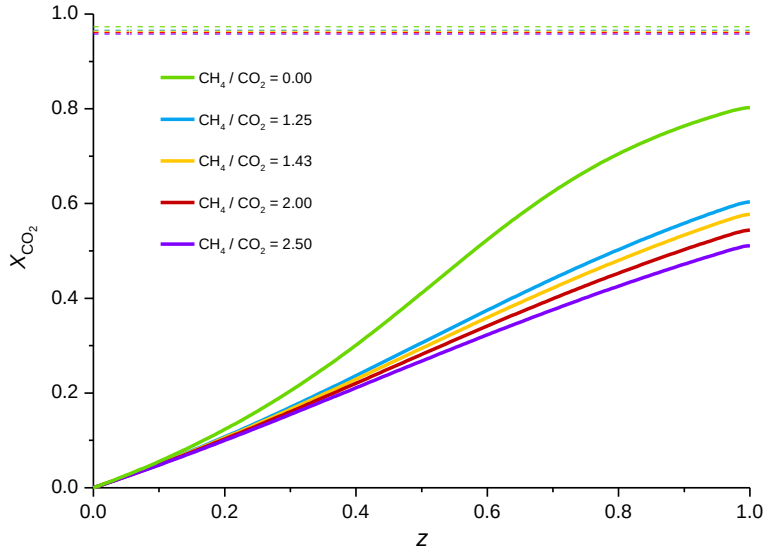


Fig. 4.4 - Effect of the biogas composition ($\mathrm{CH_4/CO_2}$ ratio) for $P = 1$ bar; $T = 250$ ºC, $Q_{\mathrm{STP}}/W_{\mathrm{cat}} = 40$ $\mathrm{mL_{STP}{\cdot}min^{-1}{\cdot}g_{cat}^{-1}}$ and $\mathrm{H_2/CO_2}$ ratio of 4. Dotted lines stand for respective thermodynamic limit, calculated based on feed conditions (*cf.* Appendix B).

It was found that $X_{CO_2}$ decrease with the increase of the $\mathrm{CH_4/CO_2}$ ratio since the reaction (and the corresponding kinetics) is favoured by the presence of $CO_2$ (reagent) and absence of $CH_4$ (product) – *cf*. Eq. 4.1. Indeed, the $CO_2$ conversion measured at the reactor outlet ($z = 1$) decreases from 80 % (simulation 5 – no $CH_4$) to 51 - 60 % depending on the content of $CH_4$ in the feed (simulations 1 to 4).

### 4.3.2.2 Effect of $\mathrm{H_2/CO_2}$ ratio

Still regarding the effect of the feed composition, also the influence of $\mathrm{H_2/CO_2}$ ratio was evaluated (simulations 1, 6 and 7), as shown in Fig. 4.5.

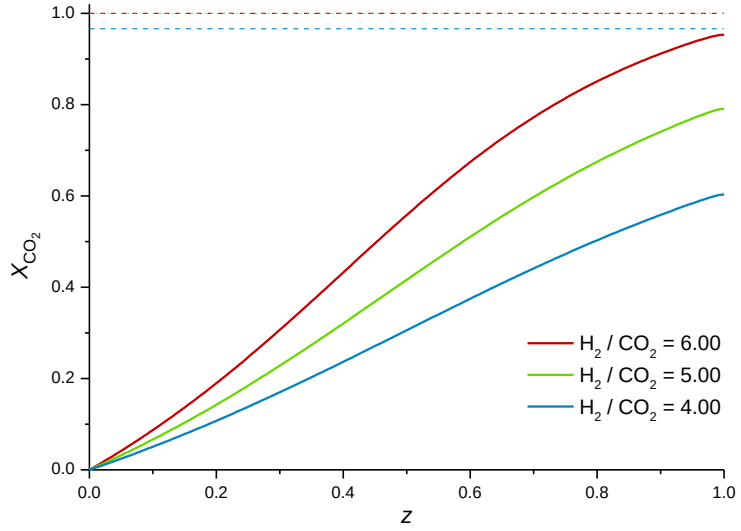


Fig. 4.5 - Effect of $\mathrm{H_2/CO_2}$ ratio for $P = 1$ bar; $T = 250$ ºC, $Q_{\mathrm{STP}}/W_{\mathrm{cat}} = 40$ $\mathrm{mL_{STP}{\cdot}min^{-1}{\cdot}g_{cat}^{-1}}$ and $\mathrm{CH_4/CO_2}$ ratio of 1.25. Dotted lines stand for respective thermodynamic limits (*cf.* Appendix B).

Increasing the $H_2/CO_2$ ratio from 4 to 5 (simulations 1 and 6, respectively) or to 6 (simulation 7), significantly enhances $CO_2$ conversion, which would be anticipated based on the reaction kinetic (Eq. 4.1). It should be noted, however, that the process might become less and less economically viable as the amount of $H_2$ in the feed is increased due to the high cost of this reagent.

#### 4.3.2.3 Effect of pressure

The effect of the pressure, evaluated by simulation 1 and 8, is represented in Fig. 4.6.

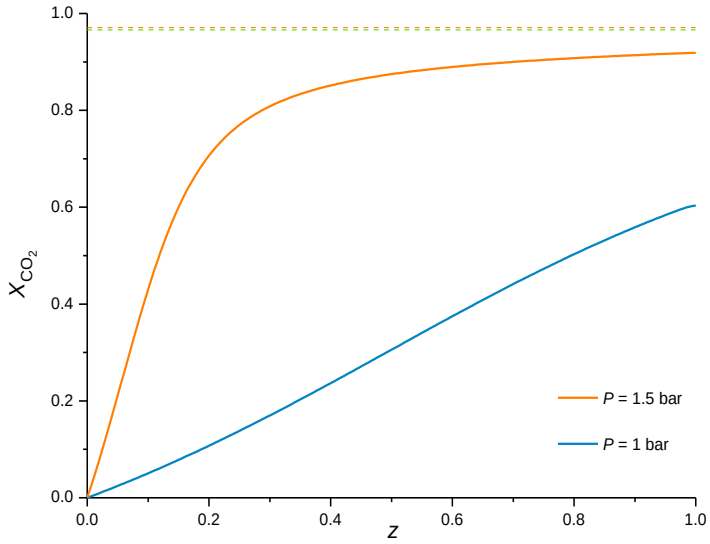


Fig. 4.6 - Effect of pressure for $T = 250$ ºC, $Q_{STP}/W_{cat} = 40$ $mL_{STP}{\cdot}min^{-1}{\cdot}g_{cat}^{-1}$, $CH_4/CO_2$ ratio of 1.25 and $H_2/CO_2$ ratio of 4. Dotted lines stand for respective thermodynamic limit (*cf.* Appendix B).

Comparing simulation 1 to simulation 8, great improvements in $X_{CO_2}$ are verified when using slightly higher pressure. This was to be expected since, according to the Le Chatelier principle, the increase in pressure (volume contraction) leads the equilibrium to shift towards the side with the least number of moles, which in this case is towards the forward direction. However, the most important effect of the total pressure increase from 1 to 1.5 bar is not in the thermodynamics (see dotted lines in Fig. 4.6) but rather in the reaction kinetics, so that $CO_2$ conversion approaches the equilibrium conversion in a shorter reaction length. Note that higher pressures have not been simulated because an increase of only 0.5 bar (from 1 to 1.5 bar) remarkably increases the $CO_2$ conversion, almost reaching the equilibrium conversion.

#### 4.3.2.4 Effect of temperature

The influence of the temperature is shown in Fig. 4.7.

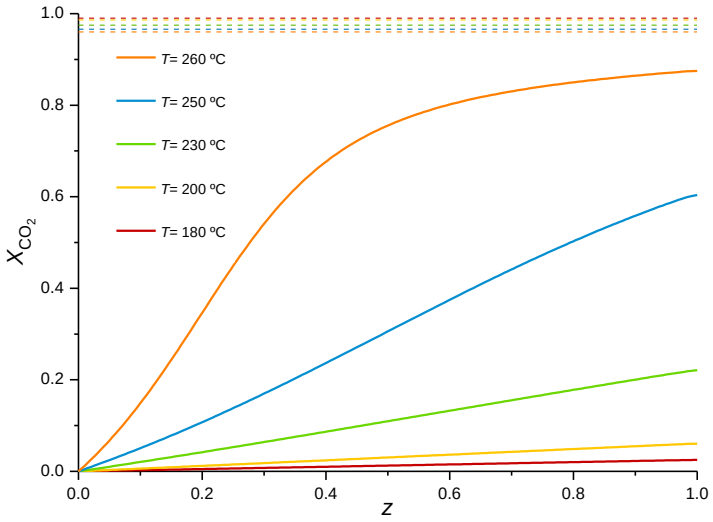


Fig. 4.7 - Effect of temperature for $P = 1$ bar, $Q_{STP}/W_{cat} = 40$ $mL_{STP}{\cdot}min^{-1}{\cdot}g_{cat}^{-1}$, $CH_4/CO_2$ ratio of 1.25 and $H_2/CO_2$ ratio of 4. Dotted lines stand for respective thermodynamic limit (*cf.* Appendix B).

Since methanation is an exothermic reaction, the operating temperature will have to be high enough for the catalyst achieving the appropriate activity to establish a reaction front - kinetically viable - but low enough to prevail the reaction in the forward direction - thermodynamically viable. Fig. 4.7 shows that $X_{CO_2}$ increases with temperature, while the equilibrium conversion (thermodynamic limit) decreases. Moreover, it was shown that the increment of $X_{CO_2}$ is progressively more pronounced at higher temperatures (particularly above 230 ºC).

#### 4.3.2.5 Effect of space velocity

The space velocity establishes the relationship between the total flow rate ($Q_{STP}$) and the catalyst mass ($W_{cat}$). The influence of the space velocity is illustrated in Fig. 4.8 - simulations 1 and 13 to 18.

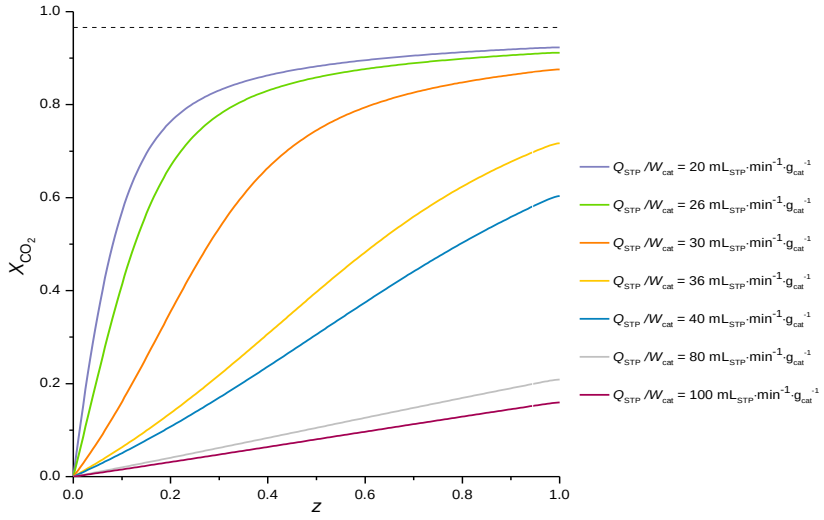


Fig. 4.8 - Effect of space velocity for $P = 1$ bar, $T = 250$ ºC, $CH_4/CO_2$ ratio of 1.25 and $H_2/CO_2$ ratio of 4. Dotted line stands for thermodynamic limit (*cf.* Appendix B).

Fig. 4.8 shows that, while space velocity decreases (i.e. $Q_{\mathrm{STP}}$ decreases or $W_{\mathrm{cat}}$ increases), $X_{\mathrm{CO_2}}$ considerably increases due to the longer contact time between reactant species with the catalyst within the reactor. With the lowest simulated space velocity (20 $mL_{STP} \cdot min^{-1} \cdot g_{cat}^{-1}$) - higher residence time -, the maximum achieved conversion is very close to the equilibrium conversion defined by the thermodynamic limit (and calculated based on feed conditions).

### 4.3.3 Evolution of relevant variables along the reactor length

For a more careful analysis of the evolution of some important variables along the reactor length, two simulations whose results are representative were chosen: simulation 1 (the reference simulation, at 1 bar) and simulation 8 (at 1.5 bar) that presents more pronounced responses, representing the reactions that achieve $CO_2$ conversions closer to equilibrium.

The evolution of the molar fractions of each component $i$ ($y_i$) for both simulations are presented in Fig. 4.9.

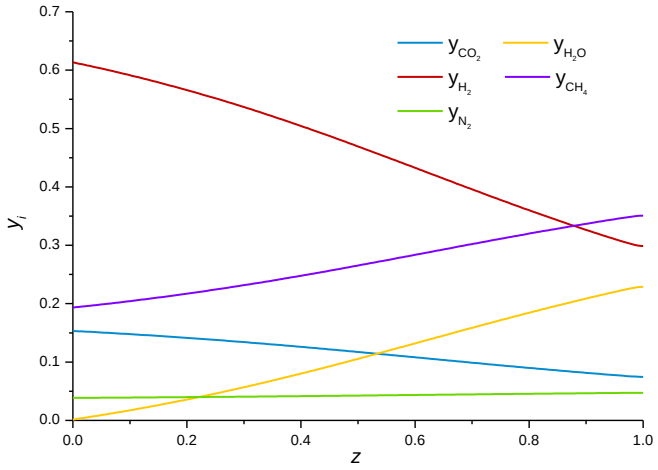


a)

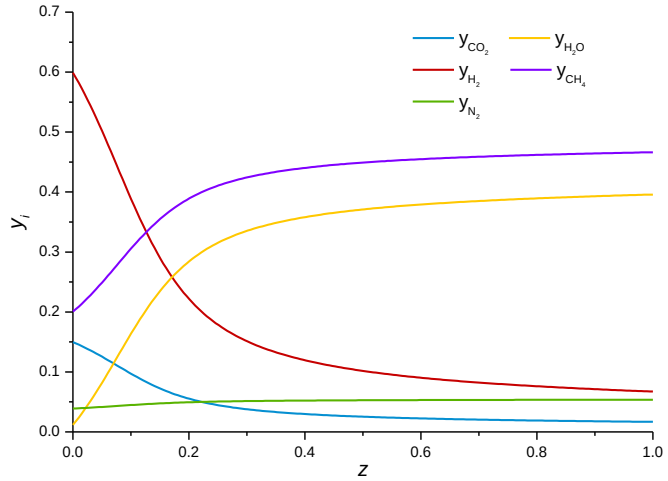


b)

Fig. 4.9 - Evolution of the molar fractions of each component $i$ along the reactor for simulation 1 (a) and for simulation 8 (b).

Fig. 4.9 shows a decrease in the quantity of reagents ($CO_2$ and $H_2$) and, consequently, an increase in the fraction of products ($CH_4$ and $H_2O$). However, for simulation 8 it is verified that the activity is much more pronounced, especially at the beginning of the reactor (approximately up to 25 % of the reactor length), due to the increased reaction kinetics when changing the pressure from 1 to 1.5 bar, as discussed above.

The slight increase in the $N_2$ fraction along the reactor length is explained by the fact that during the reaction there is a reduction in the number of moles and, as it does not participate in the reaction, its relative quantity in the mixture increases. For simulation 8, the increase in the $N_2$ fraction is more notable because the conversion of the reagents is higher.

These findings are consistent with what is observed regarding the temperature ($T$) and superficial velocity ($u_0$), as illustrated in Fig. 4.10 and Fig. 4.11, respectively.

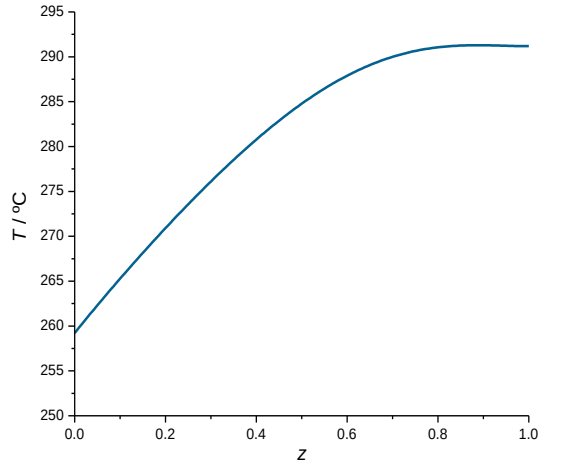


a)

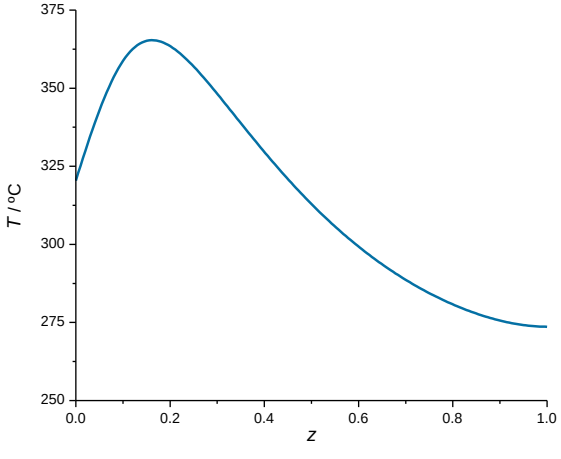


b)

Fig. 4.10 - Evolution of temperature along the reactor for simulation 1 (a) and for simulation 8 (b).

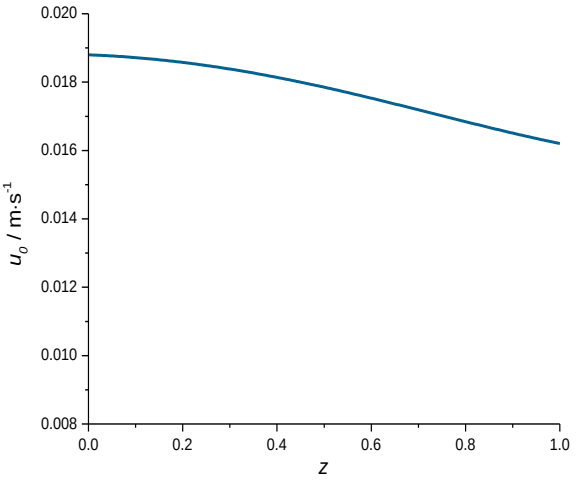


a)

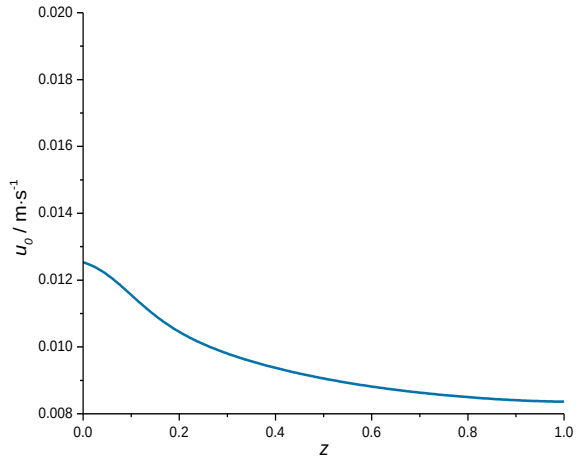


b)

Fig. 4.11 - Evolution of superficial velocity along the reactor for simulation 1 (a) and for simulation 8 (b).

Fig. 4.10 shows that the temperature increases to a maximum due to the energy released by the exothermic reaction. Thereafter, the reaction rate decreases and the energy released by the reaction does not compensate the loses through the reactor wall, so that $T$ decreases as well. For $P = 1.5$ bar (simulation 8), this behaviour is more evident being observed the occurrence of a hot spot located at $z = 0.16$. This highlights the effect of pressure, which improves the conversion from the thermodynamic point of view, because methanation takes place with a decrease of the number of moles, and also from the reaction kinetics.

Fig. 4.11 shows that the superficial velocity decreases along the reactor length because the methanation occurs with a decrease of the number of moles (from 5 to 3), as already mentioned above. Although the standard volumetric flow rate is the same for both simulations (and consequently the same molar flow rate), the volumetric flow rate adjusted to the considered $P$ and $T$ conditions decreases with increasing pressure. This results in a decrease in superficial velocity, explaining the lower values observed for simulation 8.

Table 4.5 – Operating conditions considered in the simulations and respective $CO_2$ conversion at the reactor outlet.

| | Simulation | 1 | 2 | 3 | 4 | 5 | 6 | 7 | 8 |
|---|---|---|---|---|---|---|---|---|---|
| Input | $T$ (ºC) | 250 | - | - | - | - | - | - | - |
| | $P$ (bar) | 1.00 | - | - | - | - | - | - | 1.50 |
| | $Q_{STP}/W_{cat}$ ($mL_{STP}\cdot min^{-1}\cdot g_{cat}^{-1}$) | 40.0 | - | - | - | - | - | - | - |
| | $y_{CO_2}$ | 0.154 | 0.146 | 0.136 | 0.122 | 0.180 | 0.133 | 0.118 | 0.154 |
| | $y_{H_2}$ | 0.615 | 0.588 | 0.546 | 0.490 | 0.720 | 0.667 | 0.706 | 0.615 |
| | $y_{CH_4}$ | 0.192 | 0.208 | 0.273 | 0.306 | 0.000 | 0.167 | 0.147 | 0.192 |
| | $y_{H_2O}$ | 0.000 | - | - | - | - | - | - | 0.000 |
| | $y_{N_2}$ | 0.0390 | 0.0580 | 0.0450 | 0.0820 | 0.100 | 0.0330 | 0.0290 | 0.0390 |
| | $H_2/CO_2$ ratio | 4.00 | - | - | - | - | 5.00 | 6.00 | 4.00 |
| | $CH_4/CO_2$ ratio | 1.25 | 1.43 | 2.00 | 2.50 | 0.00 | 1.25 | - | 1.25 |
| Output | $X_{CO_2}$ (%) | 60.4 | 57.7 | 54.4 | 51.1 | 80.3 | 79.1 | 95.3 | 91.9 |

| | Simulation | 9 | 10 | 11 | 12 | 13 | 14 | 15 | 16 | 17 | 18 |
|---|---|---|---|---|---|---|---|---|---|---|---|
| Input | $T$ (ºC) | 180 | 200 | 230 | 260 | 250 | - | - | - | - | - |
| | $P$ (bar) | 1.00 | - | - | - | - | - | - | - | - | - |
| | $Q_{STP}/W_{cat}$ ($mL_{STP}\cdot min^{-1}\cdot g_{cat}^{-1}$) | 40.0 | - | - | - | 20.0 | 26.0 | 30.0 | 36.0 | 80.0 | 100 |
| | $y_{CO_2}$ | 0.154 | - | - | - | - | - | - | - | - | - |
| | $y_{H_2}$ | 0.615 | - | - | - | - | - | - | - | - | - |
| | $y_{CH_4}$ | 0.192 | - | - | - | - | - | - | - | - | - |
| | $y_{H_2O}$ | 0.000 | - | - | - | - | - | - | - | - | - |
| | $y_{N_2}$ | 0.0390 | - | - | - | - | - | - | - | - | - |
| | $H_2/CO_2$ ratio | 4.00 | - | - | - | - | - | - | - | - | - |
| | $CH_4/CO_2$ ratio | 1.25 | - | - | - | - | - | - | - | - | - |
| Output | $X_{CO_2}$ (%) | 2.51 | 6.05 | 22.1 | 87.5 | 92.3 | 91.2 | 87.6 | 71.7 | 20.9 | 16.0 |

## 4.4 Sorption-enhanced reactor

The results of a preliminary test using a 50 $cm^3$ reactor packed with a mixture of 0.5 wt.%Ru/$Al_2O_3$ catalyst and zeolite 4AK for demonstration of the sorption-enhanced reactor are shown in Fig. 4.12. The feed composition consisted of 10 % of $CO_2$ and 40 % of $H_2$ balanced in nitrogen.[b)]

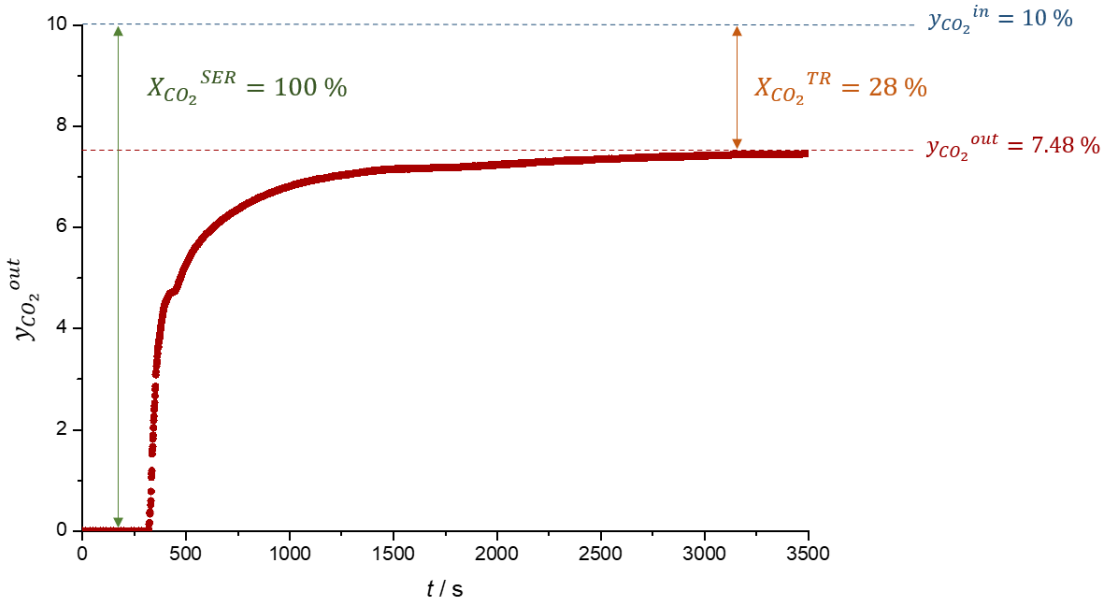


Fig. 4.12 - $CO_2$ breakthrough curve experimentally obtained with a SER.

Until 320 s there is no $CO_2$ leaving the reactor because the produced water is being adsorbed in the zeolite, favouring the reaction in the forward direction and promoting the total conversion of $CO_2$. However, when the sorbent starts reaching its saturation, it loses its adsorption capacity and there is no more *in-situ* water removal. Therefore, the reaction equilibrium is no longer shifted in the forward direction and some $CO_2$ starts leaving the reactor; ultimately, i.e. in steady-state, the SER starts behaving like a traditional reactor – in the plateau of the breakthrough curve (*cf*. Fig. 4.12).

To evaluate other important parameters (e.g. the $CH_4$ purity), further experiments with a gas analyser that can measure the composition of all species at the outlet of the reactor are required. For this reason, the $CO_2$ conversion corresponding to the traditional reactor (i.e. the region of the breakthrough tail) had to be estimated through reactor simulation, because the composition of the outlet stream was not measured (only of $CO_2$). The simulation considered the same reactor

[b)] The predicted experimental part of this work had to be cancelled due to the COVID-19 outbreak. The experimental data discussed in this section were obtained in December 2019 and kindly provided by Joana Martins (Power2Methane project researcher at LEPABE).

dimensions, feed composition, space velocity, temperature, pressure and bed porosity of the SER tested. However, to estimate $CO_2$ conversion of the TR, it was necessary to adjust the kinetic law taking into account some considerations. To ensure that the catalyst activation is fully achieved the temperature should be raised to 300 ºC based on TPR results; in this work the activation was performed until 250 ºC. For this reason, it could be expected that the kinetics determined by Falbo *et al*.[44] are higher since activation was performed at 400 ºC. Besides, thermodynamic studies predict that the in-situ water removal favours the coke formation (cf. Eq. 4.3), which would also limit the activity of the catalyst.

$$CO_2 + 2H_2 \rightleftarrows C + 2H_2O \qquad \text{Eq. 4.3}$$

Thus, in this simulation the kinetics determined by Falbo *et. al*[44] had to be multiplied by a factor of 0.35 and the obtained $CO_2$ conversion was found to be 28 %.

Fig. 4.13 represents the evolution of temperature along the reactor length based on the experimental data (SER in steady-state) and the simulation results (TR).

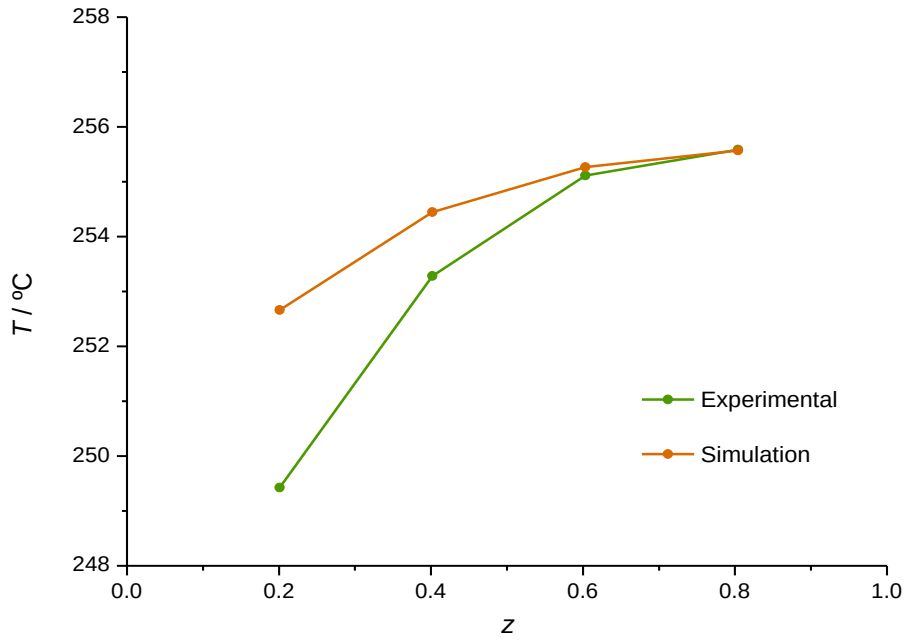


Fig. 4.13 - Evolution of temperature along the reactor based on experimental data and simulation results.

Fig. 4.13 shows that the experimental values of temperature in four positions of the reactor can be quite well predicted by the model, particularly for higher lengths.

Hence, the advantage of using a SER is that, for the considered operation conditions, $CO_2$ conversion can be enhanced from 28 % (value obtained from simulation of the TR) to 100 % (i.e. conversion obtained experimentally in the SER during the initial 320 seconds). The main

disadvantage is that it requires at least two units for continuous operation (i.e. while one is producing methane, the other is regenerating the sorbent).

## 4.5 Adsorbent materials

In this section, information of different zeolites was retrieved from literature to identify promising water-selective adsorbents for future work. Table 4.6 lists the considered zeolites.

Table 4.6 - Different types of considered zeolites.

| Zeolite | Particle size / Pore size | Supplier | Studied species | Reference |
|---|---|---|---|---|
| **3A** | Beads: 1/16 in<br>Pore size: 3 Å | Sigma Aldrich, USA | $H_2O$ | [60] |
| **4A** BFK | Beads: (1.6-2.5) mm<br>Pore size: 4 Å | Chemiewerk Bad Köstritz, Germany | $H_2O$, $CO_2$, $CH_4$, $N_2$ | [48] |
| **13X** BFK | Beads: (1.6-2.5) mm<br>Pore size: 9 Å | Chemiewerk Bad Köstritz, Germany | $H_2O$, $CO_2$, $CH_4$ | [61, 62] |

Collected information includes high temperature adsorption equilibrium values and isotherm models. For cases in which the later was not available, experimental data were fitted against the simple Freundlich adsorption isotherm model (Eq. 4.4)[63].

$$q = K_{\mathrm{F}}\, p^{1/n} \qquad \text{Eq. 4.4}$$

In Eq. 4.4, $q$ stands for the amount adsorbed (mol·kg$^{-1}$), $K_F$ is the Freundlich adsorption constant (mol·kg$^{-1}$·Pa$^{-1/n}$) and $n$ is a dimensionless empirical constant.

$K_F$ and $n$ are temperature dependent according to Eq. 4.5 and Eq. 4.6[63], respectively.

$$K_{\mathrm{F}} = K_0 \exp\left(\alpha\, \beta\, T\right) \qquad \text{Eq. 4.5}$$

$$\frac{1}{n} = \beta\, T \qquad \text{Eq. 4.6}$$

$K_0$ represents the pre-exponencial factor of the adsorption equilibrium constant and the parameter $\beta$ stands for a constant parameter related to the characteristic adsorption potential[63]. $\alpha$ is the coefficient $A$ of the Antoine equation (temperature in K and pressure in Pa) in Neperian logarithm form, which for water, in a temperature range between 99 ºC and 374 ºC, corresponds to 23.6[64].

The fitted isotherm parameters were estimated with a MATLAB® nonlinear regression algorithm based on Levenberg-Marquardt method for the minimization of the sum of residuals squares. Those values were statistically tested for 95 % level of significance with the *fitnlm* function available in MATLAB®, obtaining $t_{stat}$ and $p - value$. $t_{stat}$ represents the ratio between the estimated parameter value and the associated standard error. A $p - value < 0.05$ is statistically significant, indicating a strong evidence against the null hypothesis.

In the subsections below, the water adsorption capacity for different zeolites at the same temperature is compared; estimated adsorption equilibrium isotherms for temperatures of interest for SER and corresponding parameters are presented; and selectivity of the materials to the different species involved in the process is detailed.

### 4.5.1 Comparison of the water capacity of selected zeolites

The adsorption capacity of selected zeolites was evaluated comparing experimental adsorption equilibrium data.

Fig. 4.14 shows the amount of water adsorption with water partial pressure for the three zeolites at 100 ºC and at 250 - 260 ºC, a temperature of interest for SER.

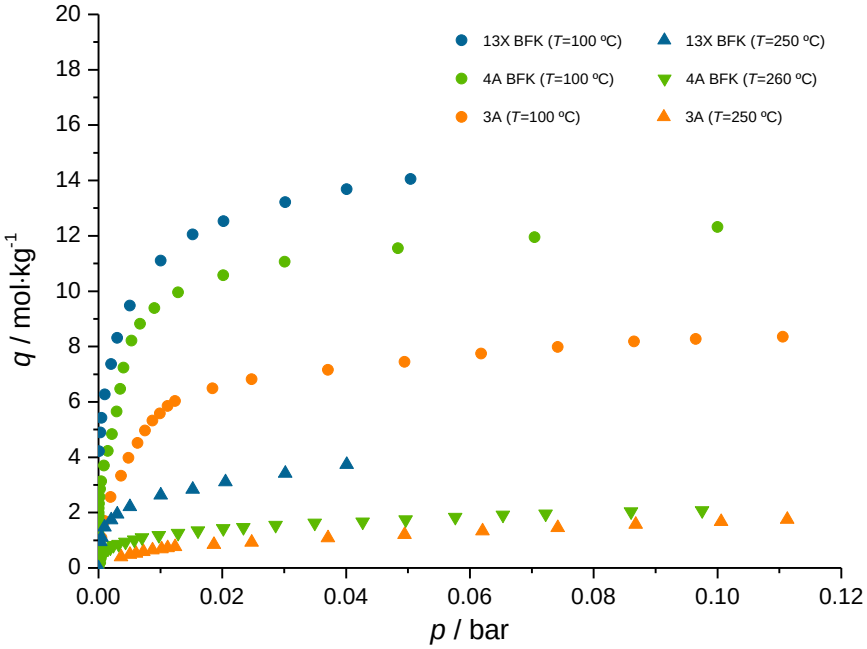


Fig. 4.14 - Water adsorption on zeolites 3A, 4A BFK and 13X BFK at 100 ºC (●), 250 ºC (▲) and 260 ºC (▼).

Fig. 4.14 shows that zeolite 13X BFK presents the highest adsorption capacity and zeolite 3A the lowest. However, zeolites 13X and 4A presented herein are binder-free (BF) and, therefore, their sorption capacity can be about 18 - 20 wt.% higher than that of binder-containing zeolites[50], while

for zeolite 3A the decrease of the adsorption capacity due to the binder is already considered. Even so, it is anticipated that this effect *per se* is not enough to justify the differences observed in Fig. 4.14.

In what concerns temperature influence, it is observed that water adsorption capacity decreases for higher temperatures due to the exothermicity of the adsorption phenomenon.

### 4.5.2 Adsorption equilibrium isotherms for water on different zeolites for temperatures of interest for SER

#### 4.5.2.1 Zeolite 3A

According to the literature[60], adsorption equilibrium data for zeolite 3A follow the Langmuir-Freundlich model (*cf.* Eq. 4.7) whose parameters, as a function of temperature (K), are obtained by Eq. 4.8, Eq. 4.9 and Eq. 4.10[60]. Table 4.7 presents the constants used to calculate the parameters.

$$q = \frac{q_{\max} K_{\mathrm{LF}} p^n}{1 + K_{\mathrm{LF}} p^{\,n}} \qquad \text{Eq. 4.7}$$

$$q_{\max} = a_0 + \frac{a_1}{T} + \frac{a_2}{T^2} \qquad \text{Eq. 4.8}$$

$$K_{\mathrm{LF}} = \exp\left(b_0 + \frac{b_1}{T} + \frac{b_2}{T^2}\right) \qquad \text{Eq. 4.9}$$

$$n = n_0 + \frac{n_1}{T} \qquad \text{Eq. 4.10}$$

In these equations, $q_{\max}$ is the maximum adsorption capacity (mol·kg$^{-1}$), $K_{\mathrm{LF}}$ is the Langmuir-Freundlich adsorption constant (bar$^{-n}$), $n$ a dimensionless empirical constant and $p$ the partial pressure of the adsorbate.

Table 4.7 - Constants used to calculate the parameters of Langmuir-Freundlich model for zeolite 3A[60].

| $a_0$ (mol·kg$^{-1}$) | $a_1$ (K$^{-1}$) | $a_2 \cdot 10^{-1}$ (K$^{-1}$) | $b_0$ (Pa$^{-1}$) | $b_1 \cdot 10^{-2}$ (K$^{-1}$) | $b_2 \cdot 10^{-1}$ (K$^{-1}$) | $n_0 \cdot 10^3$ | $n_1 \cdot 10^{-1}$ (K$^{-1}$) | $\delta$ (%) |
|---|---|---|---|---|---|---|---|---|
| 13.60 | -29.161 | 74.336 | -10.659 | 19.694 | 93.358 | -92.940 | 34.056 | 11.22 |

Fig. 4.15 illustrates the adsorption of water on zeolite 3A at different temperatures through both the experimental data and the model predicted adsorption equilibrium isotherms (based on Eq. *4.7* to Eq. 4.10 and data from Table 4.7).

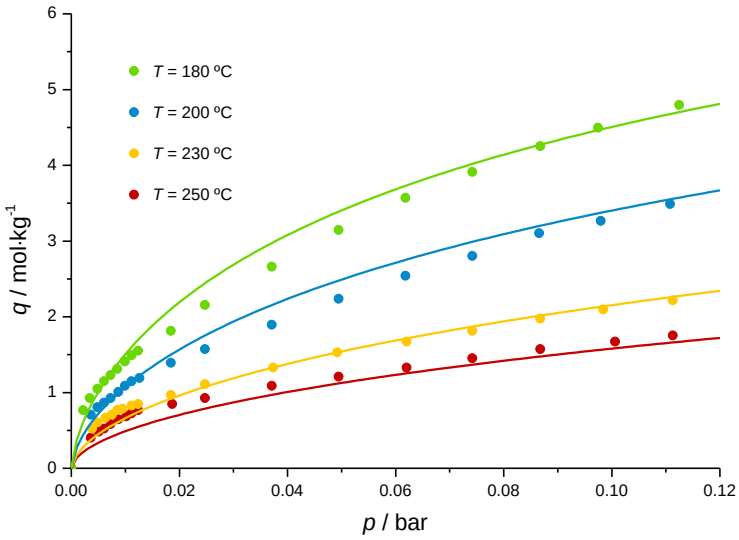


Fig. 4.15 - Adsorption of $H_2O$ over zeolite 3A through experimental data (dots) and Langmuir-Freundlich predicted model (continuous lines).

### 4.5.2.2 Zeolite 4A BFK

Adsorption equilibrium data for water on zeolite 4A BFK (from Chemiewerk Bad Köstritz, Germany) were supplied by the company and fitted against the Freundlich model (*cf.* Eq. 4.4).

The fitting parameters of the Freundlich adsorption equilibrium isotherm for water on zeolite 4A BFK and the respective statistical parameters ($t_{stat}$ and $p - Value$) are presented in Table 4.8.

Table 4.8 – Fitted constants of Freundlich adsorption isotherm for water on zeolite 4A BFK and corresponding errors (for a 95 % confidence level).

| Parameter | Value | $t_{stat}$ | $p - value$ |
|---|---|---|---|
| $K_0$ (mol·kg$^{-1}$·Pa$^{-1/n}$) | 145.9 ± 8.0 | 18.34 | $9.721 \times 10^{-37}$ |
| $\beta$ (K$^{-1}$) | $(5.396 \pm 0.069) \times 10^{-4}$ | 78.11 | $2.190 \times 10^{-105}$ |

For both $K_0$ and $\beta$, the respective $p - value$ is much lower than 0.05 (*cf.* Table 4.8), which means that is statistically significant.

Fig. 4.16 shows the adsorption isotherms for water on zeolite 4A BFK at different temperatures through both the experimental data and the model predicted adsorption equilibrium isotherms (based on Eq. 4.4 to Eq. 4.6 and data from Table 4.8).

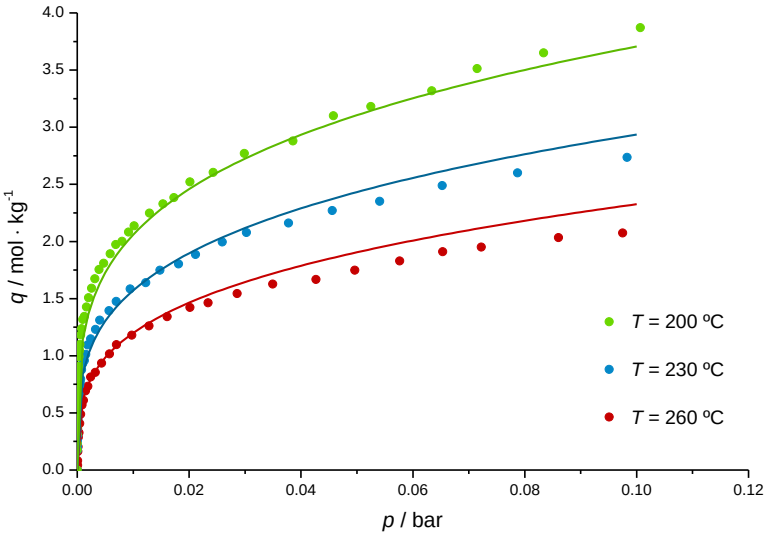


Fig. 4.16 - Adsorption of $H_2O$ over zeolite 4A BFK through experimental data (dots) and Freundlich predicted model (continuous lines).

### 4.5.2.3 Zeolite 13X BFK

Adsorption equilibrium data for water on zeolite 13X BFK, collected from literature[62], were also fitted against the Freundlich model (*cf.* Eq. 4.4).

The fitting parameters of the Freundlich adsorption equilibrium isotherm for water on zeolite 13X BFK and the respective statistical parameters ($t_{stat}$ and $p - Value$) are given in Table 4.9.

Table 4.9 – Fitted constants of Freundlich adsorption isotherm for water on zeolite 13X BFK and corresponding errors (for a 95 % confidence level).

| Parameter | Value | $t_{stat}$ | $p - Value$ |
|---|---|---|---|
| $K_0$ (mol·kg$^{-1}$·Pa$^{-1/n}$) | 201.2 ± 8.3 | 24.26 | $6.944 \times 10^{-18}$ |
| $\beta$ (K$^{-1}$) | $(4.971 \pm 0.054) \times 10^{-4}$ | 92.36 | $4.547 \times 10^{-31}$ |

For both $K_0$ and $\beta$, the respective $p - value$ is much lower than 0.05 (*cf.* Table 4.9), which means that is statistically significant.

Fig. 4.17 shows the adsorption isotherms for water on zeolite 13X at two different temperatures, through both the experimental data and the model predicted adsorption equilibrium isotherms (based on Eq. 4.4 to Eq. 4.6 and data from Table 4.9).

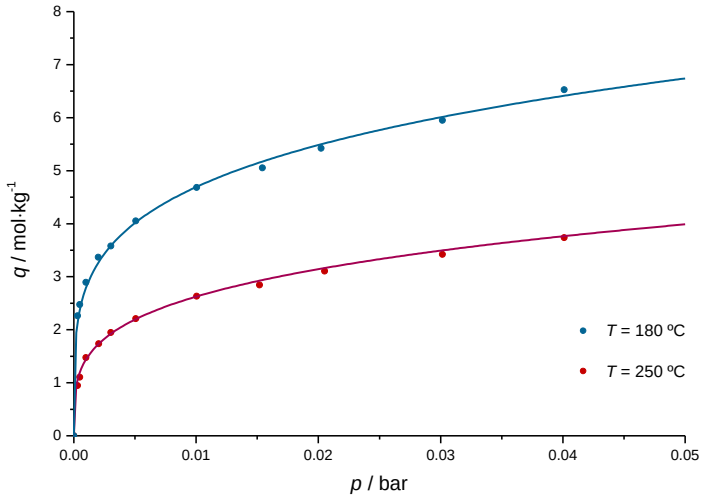


Fig. 4.17 - Adsorption of $H_2O$ over zeolite 13X BFK through experimental data (dots) and Freundlich predicted model (continuous lines).

### 4.5.3 The water selectivity of the zeolites

The (ideal) water selectivity of the zeolites regarding other relevant species involved in the process (e.g. $CO_2$, $CH_4$ and $N_2$) was studied based on single-component adsorption equilibrium data collected from the literature[48, 61, 62]. Only zeolites 4A BFK and 13X BFK were addressed in this section as they are the most promising regarding water adsorption capacity (*cf.* section 4.5.1). Detailed information and respective fitting parameters used to represent the model predicted adsorption equilibrium isotherms for all the species considered in this section are presented in Appendix C.

Please note that the available data correspond to 100 ºC, which is a temperature much lower than those experimentally used for SER. Therefore, it should be bear in mind that, for the context under study, the conclusions about the selectivity of the materials are limited.

Fig. 4.18 illustrates the water adsorption over zeolites 4A BFK (a) and 13X BFK (b) at 100 ºC.

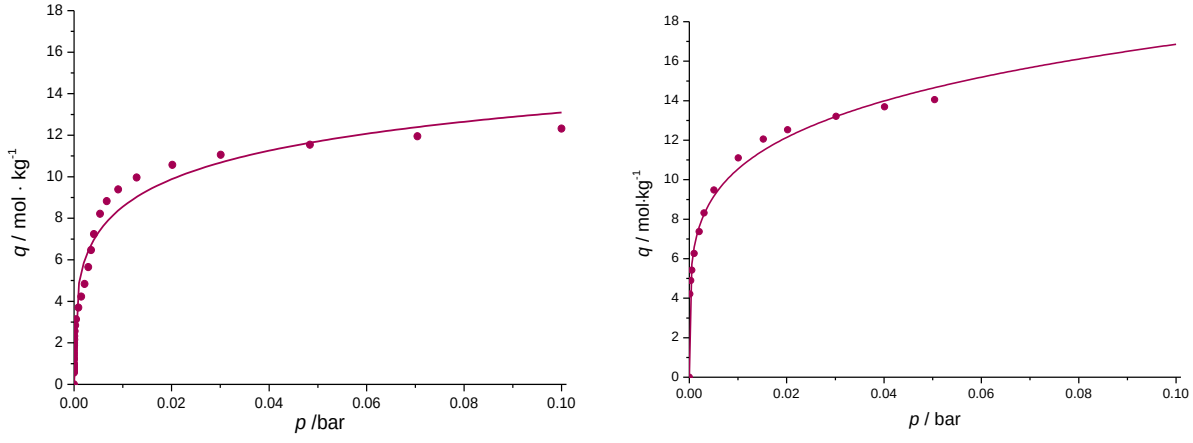


a) b)

Fig. 4.18 – Adsorption of $H_2O$ over zeolites 4A BFK (a) and 13X BFK (b) at 100 ºC.

Fig. 4.19 allows comparing the amount adsorbed of relevant species such as $CO_2$, $CH_4$ and $N_2$ over zeolite 4A BFK (top) and zeolite 13X BFK (bottom), at 100 ºC and partial pressures up to 20 bar.

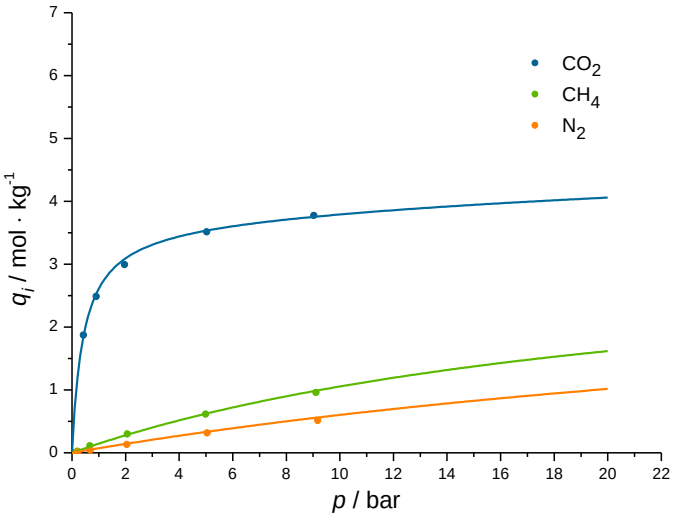


a)

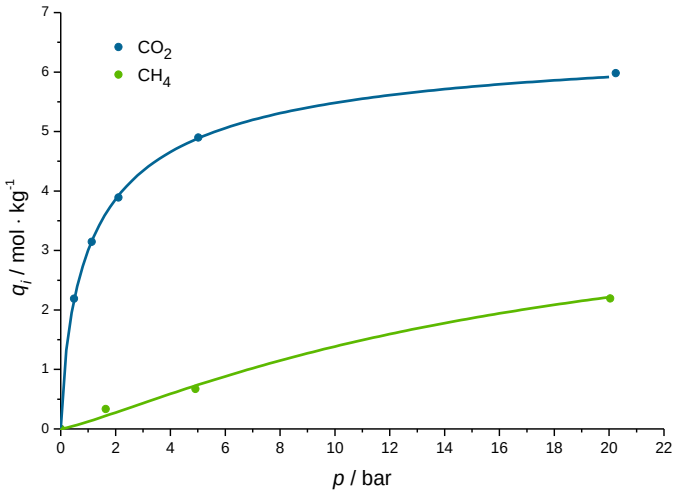


b)

Fig. 4.19 - Adsorption of $CO_2$, $CH_4$ and $N_2$ over zeolite 4A BFK (top) and $CO_2$ and $CH_4$ over zeolite 13 BFK (bottom), at $T = 100$ ºC. Lines are model predictions (see Appendix C for details).

Fig. 4.19 shows that the zeolites have affinity to the considered species decreasing in the following order: $CO_2$ > $CH_4$ > $N_2$ in the entire range of pressure.

The comparison of zeolites affinity for water compared with the abovementioned species was assessed in the pressure range between 0 - 1.5 bar, assuming that the adsorption equilibrium isotherm for water over both zeolites also applies in such a wider pressure range (*cf*. Fig. 4.20). The ideal water selectivity of the zeolites 4A BFK and 13X BFK regarding $CO_2$, $CH_4$ and $N_2$ was also determined through $q_{H_2O}/q_i$ ratio and it is represented in Fig. 4.21.

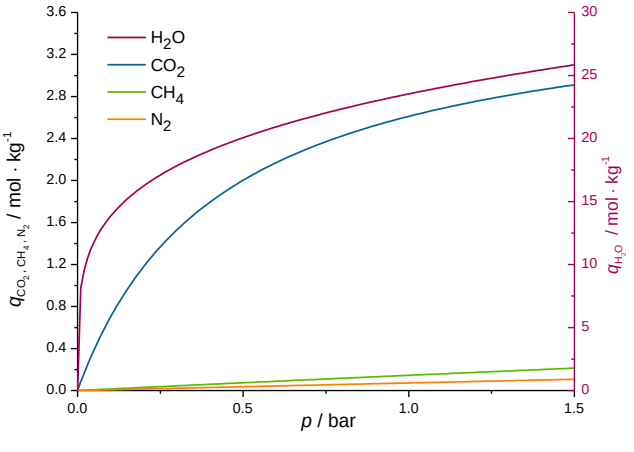


a)

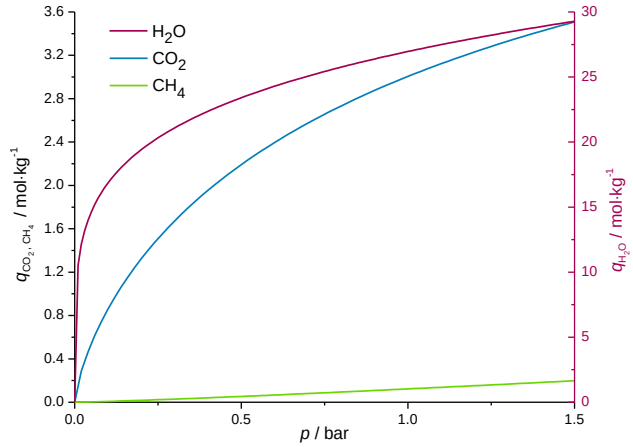


b)

Fig. 4.20 - Model predicted adsorption equilibrium isotherms of $H_2O$, $CO_2$, $CH_4$ and $N_2$ over zeolites 4A BFK (a) and 13X BFK (b) [$p = (0 - 1.5)$ bar].

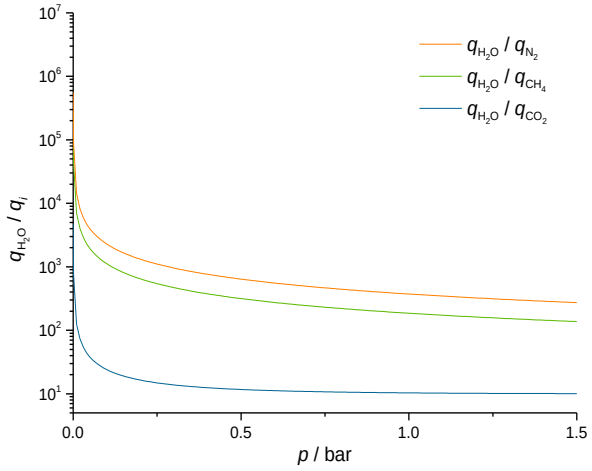


a)

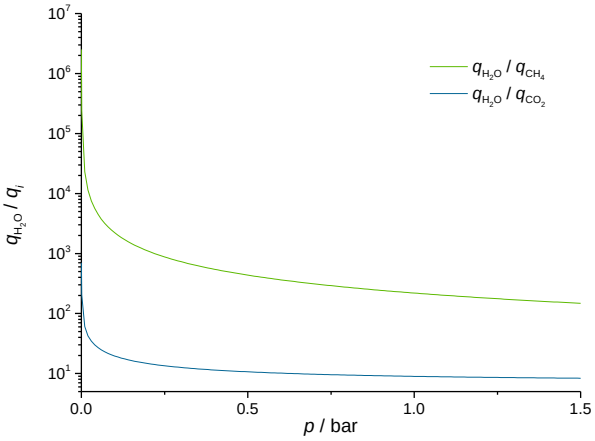


b)

Fig. 4.21 – Ideal water selectivity of the zeolites 4A BFK (a) and 13X BFK (b) regarding $CO_2$, $CH_4$ and $N_2$ [$p = (0 - 1.5)$ bar].

Fig. 4.20 shows that both zeolites display a greater affinity to water compared to the other components (please notice the different scales in both left and right axis). Fig. 4.21 corroborates the previous conclusions, showing a great ideal selectivity of the zeolites for water over the other components, which increases in the following order: $CO_2 < CH_4 < N_2$ for the entire considered pressure range.

Thus, if the behaviour of the materials remains at higher temperatures, it appears that zeolites are suitable for sorption-enhanced methanation since they have a high selectivity for $H_2O$ concerning the other species involved in the process, particularly at low partial pressures.

# 5 Conclusions

In this work a parametric study was performed through simulation of a traditional fixed bed reactor to identify the most promising operating conditions, i.e., those in which the SER could be effectively more advantageous than the TR (i.e. cases where conversion is low and far from the thermodynamic equilibrium). The effect of feed composition ($y_i$) - $\mathrm{CH_4/CO_2}$ and $\mathrm{H_2/CO_2}$ ratios -, pressure ($P$), temperature ($T$) and space velocity ($Q_{\mathrm{STP}}/W_{\mathrm{cat}}$) on $CO_2$ conversion was evaluated, being verified that it is higher for lower values of the $\mathrm{CH_4/CO_2}$ ratio and space velocity and for higher values of the $\mathrm{H_2/CO_2}$ ratio, $P$ and $T$. The evolution of some important variables along the reactor length was analysed based on two simulations that only differed in the considered total pressure ($P = 1$ bar and $P = 1.5$ bar). Comparing the molar fractions, superficial velocity and temperature profiles for the two simulations, it appears that for $P = 1.5$ bar, the behaviour is much more pronounced, highlighting the pressure effect.

The sorption-enhanced reactor concept applied to methanation was illustrated based on preliminary results and compared to a simulated traditional reactor under the same conditions. The benefit of using a SER was clear, allowing to enhanced $CO_2$ conversion from 28 % conversion to 100 % before the breakthrough time.

Adsorption equilibrium data of selected zeolites were retrieved from literature and discussed to identify the best water-selective adsorbents to consider in future work. It was found that zeolite 13X BFK is the one among those considered with the highest water adsorption capacity when compared to zeolites 3A and 4A BFK. Adsorption equilibrium isotherms and corresponding parameters for all zeolites were given/estimated in a temperature range of interest for SER that can be used in future work for modelling the sorption-enhanced-reactor. Both zeolites 13X and 4A present great affinity to water compared to $CO_2$, $CH_4$ and $N_2$, at least at 100 ºC and particularly at low partial pressures.

# 6 Evaluation of the developed work

## 6.1 Expected objectives of this work

This dissertation targeted the experimental study of an adsorptive reactor for $CO_2$ methanation. The research methodology included performing reaction and sorption-enhanced reaction experiments using a fixed-bed reactor packed with a catalyst only and with a mixed bed of a catalyst and zeolite, respectively. The goal was to check how the SER could outperform the TR in conditions where the reaction is limited, such as in biogas upgrading, where the feed contains a significant amount of $CH_4$ (a reaction product). However, the research methodology had to be adapted due to the COVID-19 outbreak and the impossibility of be present in the laboratory to perform the experimental work. In this regard, the work focused on performing simulations of a traditional reactor to study the influence of some operating conditions, allowing to verify the most promising ones, i.e. those which would make the SER more suitable over the TR. Even so, the concept of the sorption-enhanced reactor applied to methanation was illustrated and discussed based on preliminary results performed at LEPABE before the COVID-19 outbreak and compared to those obtained through simulation of a traditional reactor under the same operating conditions, clearly showing the great benefits of the multifunctional reactor.

Finally, the research methodology was also adapted to consider a brief literature review on zeolite materials for steam adsorption, to select the best adsorbent for future work with the adsorptive reactor, considering either the water adsorption capacity and its affinity compared to other relevant species like $CO_2$, $CH_4$ and $N_2$.

## 6.2 Future work

With this dissertation it was possible to experimentally demonstrate the sorption-enhancement concept, although with some limitations as only preliminary results from a single trial were available. To verify if the SER allows overpassing the equilibrium limitations caused by the presence of methane (reaction product) on $CO_2$ conversion and to which extent, it will be necessary to perform further experimental tests considering a typical biogas feed (i.e. containing methane). Determination of high temperature adsorption equilibrium values of water and other co-existent species are also necessary to check the conditions of pressure and temperature where the selectivity towards water is higher. The easiness of zeolite regeneration either by pressure or temperature swing is another aspect that should be addressed in future work, as well as the materials stability to cyclic operation hence checking if steam removal leads to catalyst deactivation due to coke deposition.

Moreover, a techno-economic analysis to benchmark the SER with other alternatives for biogas upgrade considering the methanation reaction (i.e., pressure swing adsorption followed by a

traditional reactor or simply a traditional reactor) is also recommended, for identifying also which application(s) is(are) more interesting for the upgraded biogas by SER (e.g. injection to the gas grid, production of power or heat or use as vehicle fuel).

# 7 References


1. Solomon, S., G.-K. Plattner, R. Knutti, and P. Friedlingstein, *Irreversible climate change due to carbon dioxide emissions.* Proceedings of the national academy of sciences, 2009. **106**(6): p. 1704-1709.
2. NOAA - National Oceanic and Athmospheric Administration. *Greenhouse gases*. 2020 February 12, 2020]; Available from: https://www.ncdc.noaa.gov/monitoring-references/faq/greenhouse-gases.php.
3. Songolzadeh, M., M. Soleimani, M. Takht Ravanchi, and R. Songolzadeh, *Carbon dioxide separation from flue gases: a technological review emphasizing reduction in greenhouse gas emissions.* The Scientific World Journal, 2014.
4. NOAA Earth System Research Laboratories. *Global monitoring laboratory*. April 6, 2020 [cited 2020 June 5]; Available from: https://www.esrl.noaa.gov/gmd/ccgg/trends/global.html.
5. United Nations. *Sustainable Development Goals*. February 20, 2020 [cited 2020 April 14]; Available from: https://www.un.org/sustainabledevelopment/.
6. IRENA - International Renewable Energy Agency, *Renewable capacity statistics 2019*. 2019.
7. Estermann, T., M. Newborough, and M. Sterner, *Power-to-Gas systems for absorbing excess solar power in electricity distribution networks.* International Journal of Hydrogen Energy, 2016. **41**(32): p. 13950-13959.
8. Jürgensen, L., E.A. Ehimen, J. Born, and J.B. Holm-Nielsen, *Utilization of surplus electricity from wind power for dynamic biogas upgrading: Northern Germany case study.* Biomass and Bioenergy, 2014. **66**: p. 126-132.
9. Meylan, F.D., F.-P. Piguet, and S. Erkman, *Power-to-gas through $CO_2$ methanation: assessment of the carbon balance regarding EU directives.* Journal of Energy Storage, 2017. **11**: p. 16-24.
10. Reiter, G. and J. Lindorfer, *Global warming potential of hydrogen and methane production from renewable electricity via power-to-gas technology.* The International Journal of Life Cycle Assessment, 2015. **20**(4): p. 477-489.
11. Miguel, C.V., A. Mendes, and L.M. Madeira, *An overview of the Portuguese energy sector and perspectives for power-to-gas implementation.* Energies, 2018. **11**(12): p. 3259.
12. Götz, M., J. Lefebvre, F. Mörs, A.M. Koch, F. Graf, S. Bajohr, R. Reimert, and T. Kolb, *Renewable Power-to-Gas: a technological and economic review.* Renewable energy, 2016. **85**: p. 1371-1390.
13. Jürgensen, L., E.A. Ehimen, J. Born, and J.B. Holm-Nielsen, *Dynamic biogas upgrading based on the Sabatier process: thermodynamic and dynamic process simulation.* Bioresource technology, 2015. **178**: p. 323-329.
14. Khan, I.U., M.H.D. Othman, H. Hashim, T. Matsuura, A. Ismail, M. Rezaei-DashtArzhandi, and I.W. Azelee, *Biogas as a renewable energy fuel - a review of biogas upgrading, utilisation and storage.* Energy Conversion and Management, 2017. **150**: p. 277-294.

15. Faria, A.C., C. Miguel, and L.M. Madeira, *Thermodynamic analysis of the $CO_2$ methanation reaction with in situ water removal for biogas upgrading.* Journal of $CO_2$ Utilization, 2018. **26**: p. 271-280.

16. Weiland, P., *Biogas production: current state and perspectives.* Applied microbiology and biotechnology, 2010. **85**(4): p. 849-860.

17. European Biogas Association, *Annual Report 2019*. 2019: Brussels, Belgium.

18. Kapoor, R., P. Ghosh, M. Kumar, and V.K. Vijay, *Evaluation of biogas upgrading technologies and future perspectives: a review.* Environmental Science and Pollution Research, 2019. **26**(12): p. 11631-11661.

19. Sysadvance, *Energy Catalog*. 2019.

20. Dautzenberg, F. and M. Mukherjee, *Process intensification using multifunctional reactors.* Chemical Engineering Science, 2001. **56**(2): p. 251-267.

21. Westerterp, K., *Multifunctional reactors*, in *Energy Efficiency in Process Technology*. 1993, Springer. p. 1109-1121.

22. Carvill, B., J. Hufton, M. Anand, and S. Sircar, *Sorption-enhanced reaction process.* AIChE Journal, 1996. **42**(10): p. 2765-2772.

23. Elsner, M.P., C. Dittrich, and D.W. Agar, *Adsorptive reactors for enhancing equilibrium gas-phase reactions - two case studies.* Chemical engineering science, 2002. **57**(9): p. 1607-1619.

24. Rodrigues, A.E., Y.-j. Wu, L. Madeira, and R. Faria, *Sorption enhanced reaction processes*. Vol. 1. 2017: World Scientific.

25. Mendes, D., S. Tosti, F. Borgognoni, A. Mendes, and L.M. Madeira, *Integrated analysis of a membrane-based process for hydrogen production from ethanol steam reforming.* Catalysis Today, 2010. **156**(3-4): p. 107-117.

26. Smirniotis, P. and K. Gunugunuri, *Water gas shift reaction: research developments and applications*. 2015: Elsevier.

27. Basile, A., F. Gallucci, A. Iulianelli, M. De Falco, and S. Liguori, *Hydrogen production by ethanol steam reforming: experimental study of a Pd-Ag membrane reactor and traditional reactor behaviour.* International Journal of Chemical Reactor Engineering, 2008. **6**(1).

28. Gallucci, F., E. Fernandez, P. Corengia, and M. van Sint Annaland, *Recent advances on membranes and membrane reactors for hydrogen production.* Chemical Engineering Science, 2013. **92**: p. 40-66.

29. Gallucci, F., L. Paturzo, and A. Basile, *An experimental study of $CO_2$ hydrogenation into methanol involving a zeolite membrane reactor.* Chemical Engineering and Processing: Process Intensification, 2004. **43**(8): p. 1029-1036.

30. Struis, R. and S. Stucki, *Verification of the membrane reactor concept for the methanol synthesis.* Applied Catalysis A: General, 2001. **216**(1-2): p. 117-129.

31. Li, Z. and T.T. Tsotsis, *Methanol synthesis in a high-pressure membrane reactor with liquid sweep.* Journal of membrane science, 2019. **570**: p. 103-111.

32. Delmelle, R., J. Terreni, A. Remhof, A. Heel, J. Proost, and A. Borgschulte, *Evolution of water diffusion in a sorption-enhanced methanation catalyst.* Catalysts, 2018. **8**(9): p. 341.

33. van Kampen, J., J. Boon, F. van Berkel, J. Vente, and M. van Sint Annaland, *Steam separation enhanced reactions: review and outlook.* Chemical Engineering Journal, 2019.

34. Walspurger, S., G.D. Elzinga, J.W. Dijkstra, M. Sarić, and W.G. Haije, *Sorption enhanced methanation for substitute natural gas production: Experimental results and thermodynamic considerations.* Chemical Engineering Journal, 2014. **242**: p. 379-386.

35. Miguel, C., M. Soria, A. Mendes, and L. Madeira, *A sorptive reactor for $CO_2$ capture and conversion to renewable methane.* Chemical Engineering Journal, 2017. **322**: p. 590-602.

36. Lopez Ortiz, A. and D.P. Harrison, *Hydrogen production using sorption-enhanced reaction.* Industrial & engineering chemistry research, 2001. **40**(23): p. 5102-5109.

37. Jang, H.M., K.B. Lee, H.S. Caram, and S. Sircar, *High-purity hydrogen production through sorption enhanced water gas shift reaction using $K_2CO_3$-promoted hydrotalcite.* Chemical engineering science, 2012. **73**: p. 431-438.

38. Xie, M., Z. Zhou, Y. Qi, Z. Cheng, and W. Yuan, *Sorption-enhanced steam methane reforming by in situ $CO_2$ capture on a $CaO–Ca_9Al_6O_{18}$ sorbent.* Chemical Engineering Journal, 2012. **207**: p. 142-150.

39. Borgschulte, A., N. Gallandat, B. Probst, R. Suter, E. Callini, D. Ferri, Y. Arroyo, R. Erni, H. Geerlings, and A. Züttel, *Sorption enhanced $CO_2$ methanation.* Physical Chemistry Chemical Physics, 2013. **15**(24): p. 9620-9625.

40. Delmelle, R., R.B. Duarte, T. Franken, D. Burnat, L. Holzer, A. Borgschulte, and A. Heel, *Development of improved nickel catalysts for sorption enhanced $CO_2$ methanation.* international journal of hydrogen energy, 2016. **41**(44): p. 20185-20191.

41. Borgschulte, A., R. Delmelle, R.B. Duarte, A. Heel, P. Boillat, and E. Lehmann, *Water distribution in a sorption enhanced methanation reactor by time resolved neutron imaging.* Physical Chemistry Chemical Physics, 2016. **18**(26): p. 17217-17223.

42. Leonzio, G., *Process analysis of biological Sabatier reaction for bio-methane production.* Chemical Engineering Journal, 2016. **290**: p. 490-498.

43. Liu, J., C. Li, F. Wang, S. He, H. Chen, Y. Zhao, M. Wei, D.G. Evans, and X. Duan, *Enhanced low-temperature activity of $CO_2$ methanation over highly-dispersed Ni/$TiO_2$ catalyst.* Catalysis Science & Technology, 2013. **3**(10): p. 2627-2633.

44. Falbo, L., M. Martinelli, C.G. Visconti, L. Lietti, C. Bassano, and P. Deiana, *Kinetics of $CO_2$ methanation on a Ru-based catalyst at process conditions relevant for Power-to-Gas applications.* Applied Catalysis B: Environmental, 2018. **225**: p. 354-363.

45. Garbarino, G., P. Riani, L. Magistri, and G. Busca, *A study of the methanation of carbon dioxide on Ni/$Al_2O_3$ catalysts at atmospheric pressure.* International journal of hydrogen energy, 2014. **39**(22): p. 11557-11565.

46. Gorbach, A., M. Stegmaier, and G. Eigenberger, *Measurement and modeling of water vapor adsorption on zeolite 4A - equilibria and kinetics.* Adsorption, 2004. **10**(1): p. 29-46.

47. Bauer, J., R. Herrmann, W. Mittelbach, and W. Schwieger, *Zeolite/aluminum composite adsorbents for application in adsorption refrigeration.* International Journal of Energy Research, 2009. **33**(13): p. 1233-1249.

48. Seabra, R.A.G., *Carbon dioxide separation from industrial streams (MSc thesis)*. 2017, University of Porto: Porto, Portugal.

49. Bonenfant, D., M. Kharoune, P. Niquette, M. Mimeault, and R. Hausler, *Advances in principal factors influencing carbon dioxide adsorption on zeolites.* Science and technology of advanced materials, 2008. **9**(1): p. 013007.

50. Seabra, R., A.M. Ribeiro, K. Gleichmann, A.F. Ferreira, and A.E. Rodrigues, *Adsorption equilibrium and kinetics of carbon dioxide, methane and nitrogen on binderless zeolite 4A adsorbents.* Microporous and Mesoporous Materials, 2019. **277**: p. 105-114.

51. Zhu, W., L. Gora, A. Van den Berg, F. Kapteijn, J. Jansen, and J. Moulijn, *Water vapour separation from permanent gases by a zeolite-4A membrane.* Journal of membrane science, 2005. **253**(1-2): p. 57-66.

52. Wang, Y. and M.D. LeVan, *Adsorption equilibrium of carbon dioxide and water vapor on zeolites 5A and 13X and silica gel: pure components.* Journal of Chemical & Engineering Data, 2009. **54**(10): p. 2839-2844.

53. Santos, B.A.V.d., *Process intensification in the synthesis of the green chemical dimethyl carbonate (PhD thesis)*. 2014, University of Porto: Porto, Portugal.

54. Borgschulte, A., E. Callini, N. Stadie, Y. Arroyo, M. Rossell, R. Erni, H. Geerlings, A. Züttel, and D. Ferri, *Manipulating the reaction path of the $CO_2$ hydrogenation reaction in molecular sieves.* Catalysis Science & Technology, 2015. **5**(9): p. 4613-4621.

55. Muñoz, R., L. Meier, I. Diaz, and D. Jeison, *A review on the state-of-the-art of physical/chemical and biological technologies for biogas upgrading.* Reviews in Environmental Science and Bio/Technology, 2015. **14**(4): p. 727-759.

56. Rouquerol, J., F. Rouquerol, P. Llewellyn, G. Maurin, and K.S. Sing, *Adsorption by powders and porous solids: principles, methodology and applications*. 2013: Academic press.

57. Lowell, S., J.E. Shields, M.A. Thomas, and M. Thommes, *Characterization of porous solids and powders: surface area, pore size and density*. Vol. 16. 2012: Springer Science & Business Media.

58. Schmal, M., *Heterogeneous catalysis and its industrial applications*. 2016: Springer.

59. Nurunnabi, M., K. Murata, K. Okabe, M. Inaba, and I. Takahara, *Performance and characterization of $Ru/Al_2O_3$ and $Ru/SiO_2$ catalysts modified with Mn for Fischer–Tropsch synthesis.* Applied Catalysis A: General, 2008. **340**(2): p. 203-211.

60. Gabruś, E., J. Nastaj, P. Tabero, and T. Aleksandrzak, *Experimental studies on 3A and 4A zeolite molecular sieves regeneration in TSA process: aliphatic alcohols dewatering–water desorption.* Chemical Engineering Journal, 2015. **259**: p. 232-242.

61. Rodrigues, A.E., M.J. Regufe, A. Ferreira, J.M.R. Loureiro, Alexandre M, C.V. Miguel, L.M. Madeira, and M.A. Soria, *Cyclic Adsorption/Reaction Processes in $CO_2$ Capture and Utilisation*. 2019, LSRE-LCM.

62. Mette, B., H. Kerskes, H. Drück, and H. Müller-Steinhagen, *Experimental and numerical investigations on the water vapor adsorption isotherms and kinetics of binderless zeolite 13X.* International Journal of Heat and Mass Transfer, 2014. **71**: p. 555-561.

63. Do, D.D., *Adsorption analysis: equilibria and kinetics*. Vol. 2. 1998: Imperial college press London.

64. Wichterle, I. and J. Linek, *Antoine Vapor Pressure Constants of Pure Compounds*. 1971: Academia.

65. R. Perry, D.G., *Perry's chemical engineer's handbook*. 7 ed. 1999, New York: McGraw Hill.

66. Poling, B.E., J.M. Prausnitz, and J.P. O'connell, *The properties of gases and liquids*. Vol. 5. 2001: Mcgraw-hill New York.

67. Davidson, T.A., *Simple and accurate method for calculating viscosity of gaseous mixtures.* 1993.

68. Louro, C.S.C., *Thermal conductivity of gases: transient hot-wire method*, in *Departamento de Engenharia Química e Biológica (DEQB)*. 2008, IST, Universidade de Lisboa.

69. Wakao, N. and T. Funazkri, *Effect of fluid dispersion coefficients on particle-to-fluid mass transfer coefficients in packed beds. Correlation of Sherwood numbers.* Chemical Engineering Science, 1978. **33**(10): p. 1375-1384.

# Appendix A - Physical properties considered for the simulation MATLAB® code

The physical properties required to develop the simulation program are listed below.

- **Thermodynamic properties for each species**

Table A.1. – Molar weight, critical temperature and critical pressure for each species considered in this work[65].

| Property | $CO_2$ | $H_2$ | $H_2O$ | $CH_4$ | $N_2$ |
|---|---|---|---|---|---|
| Molar weight, $M_i$ (g·mol$^{-1}$) | 44.01 | 2.02 | 18.02 | 16.04 | 28.01 |
| Critical temperature, $T_{c,i}$ (K) | 304.2 | 33.19 | 647.1 | 190.7 | 126.2 |
| Critical pressure, $P_{c,i}$ (bar) | 73.83 | 13.13 | 220.55 | 46.00 | 34.00 |

- **Density of the gas mixture ($\rho_f$)**

$\rho_f$ is determined by Eq. A.1.

$$\rho_f = \frac{P}{R_g\, T} \sum_{i=1}^{n} (y_i\, M_i) \qquad \text{Eq. A.1}$$

where $P$ represents total pressure, $T$ is temperature, $R_g$ stands for ideal gas constant, $y_i$ is the molar fraction of species $i$ and $M_i$ is the molar weight of species $i$.

- **Specific heat capacity of the gas mixture ($C_{p,f}$)**

$C_{p,f}$ is obtained by Eq. A.2.

$$C_{p,f} = \sum_{i=1}^{n} \frac{y_i\, C_{p,i}}{M_i} \qquad \text{Eq. A.2}$$

where $C_{p,i}$ corresponds to the molar heat capacity of species $i$, calculated through Eq. A.3.

$$C_{p,i} = A_i + B_i\, T + C_i\, T^2 + D_i\, T^{-2} \qquad \text{Eq. A.3}$$

$A$-$D$ are specific coefficients for each species that are presented in Table A.2.

Table A.2 – Specific coefficients used to estimate the heat capacity of the pure species though Eq. A.3.

| Species | $A$ ($J \cdot mol^{-1} \cdot K^{-1}$) | $B \times 10^3$ ($J \cdot mol^{-1} \cdot K^{-2}$) | $C \times 10^6$ ($J \cdot mol^{-1} \cdot K^{-3}$) | $D \times 10^{-5}$ ($J \cdot mol^{-1} \cdot K$) |
|---|---|---|---|---|
| $CO_2$ | 5.457 | 1.045 | 0 | -1.157 |
| $H_2$ | 3.249 | 0.422 | 0 | 0.083 |
| $H_2O$ | 3.470 | 1.450 | 0 | 0.121 |
| $CH_4$ | 1.702 | 9.081 | -2.164 | 0 |
| $N_2$ | 3.280 | 0.593 | 0 | 0.040 |

- **Viscosity of the gas mixture ($\mu_f$)**

$\mu_f$ is estimated using the Wilke method[66] (Eq. A.4).

$$\mu_{\mathrm{f}} = \sum_{i=1}^{n} \frac{y_i \, \mu_i}{\sum_{j=1}^{n} (y_i \, \phi_{ij})} \qquad \text{Eq. A.4}$$

being $\phi_{ij}$ the binary term for the mixture of species $i$ and $j$ and $\mu_i$ the viscosity of species $i$, calculated by Eq. A.5[67] and Eq. A.6[65], respectively.

$$\phi_{ij} = \frac{\left[1 + \sqrt{\frac{\mu_i}{\mu_j}} \left(\frac{M_j}{M_i}\right)^{1/4}\right]^2}{\left[8\left(1 + \frac{M_j}{M_i}\right)\right]^{1/2}} \qquad \text{Eq. A.5}$$

$$\mu_i = \frac{A \, T^B}{1 + \frac{C}{T} + \frac{D}{T^2}} \qquad \text{Eq. A.6}$$

$A$-$D$, shown in Table A.3, are specified values for each species and were retrieved from Aspen Properties software.

Table A.3 - Coefficients to determine the pure viscosity (Pa·s) of each species.

| Species | $A$ | $B$ | $C$ | $D$ |
|---|---|---|---|---|
| $CO_2$ | $2.1480 \times 10^{-6}$ | 0.46000 | 290.000 | 0 |
| $H_2$ | $1.7970 \times 10^{-7}$ | 0.68500 | -0.590 | 140 |
| $H_2O$ | $1.7096 \times 10^{-8}$ | 1.11460 | 0.000 | 0 |
| $CH_4$ | $5.2546 \times 10^{-7}$ | 0.59006 | 105.670 | 0 |
| $N_2$ | $6.5592 \times 10^{-7}$ | 0.60810 | 54.714 | 0 |

- **Molecular diffusivity of the gas mixture ($D_{\mathrm{m,f}}$)**

Eq. A.7 allows to calculate $D_{\mathrm{m,f}}$:

$$D_{\mathrm{m,f}} = \sum_{i=1}^{n} D_{m,i}\, y_i \qquad \text{Eq. A.7}$$

being $D_{m,i}$ the molecular diffusivity of species $i$ (*cf.* Eq. A.8)[24].

$$D_{m,i} = \frac{1 - y_i}{\sum_{j=1}^{n} \frac{y_j}{D_{ij}}} \qquad \text{Eq. A.8}$$

The binary diffusivity, $D_{ij}$ , is estimated based on the Fuller method[65](Eq. A.9).

$$D_{ij} = \frac{10^{-3}\, T^{1.75} \left(\frac{1}{M_i} + \frac{1}{M_j}\right)}{P \left( (\sum v)_i^{\,1/3} + (\sum v)_j^{\,1/3} \right)^2} \qquad \text{Eq. A.9}$$

where $(\sum v)_i$ and $(\sum v)_j$ is the sum of the atomic diffusion volumes for species $i$ and $j$, respectively. The latest values are given in Table A.4.

Table A.4 - Sum of the atomic diffusion volumes for each species considered in this work.

| Molecule | Diffusion volume, $\left(\sum v\right)$, $cm^3 \cdot mol^{-1}$ |
|---|---|
| $CO_2$ | 26.9 |
| $H_2$ | 7.07 |
| $H_2O$ | 12.7 |
| $CH_4$ | 24.4 |
| $N_2$ | 17.9 |

- **Mass axial dispersion coefficient ($D_{\mathrm{ax}}$)**

$D_{\mathrm{ax}}$ is obtained by Eq. A.10:

$$D_{\mathrm{ax}} = \frac{u_0\, d_{\mathrm{p}}}{\varepsilon_{\mathrm{b}}\, Pe} \qquad \text{Eq. A.10}$$

being $d_p$ the catalyst particle diameter and $Pe$ the Péclet number (*cf.* Eq. A.11), calculated as a function of Reynolds - $Re$ - (*cf.* Eq. A.12) and Schmidt - $Sc$ - numbers (*cf.* Eq. A.13).

$$\frac{1}{Pe} = \frac{0.3\, \varepsilon_{\mathrm{b}}}{Re\, Sc} + \frac{0.5}{1 + \frac{3.8}{Re\, Sc}} \qquad \text{Eq. A.11}$$

$$Re = \frac{\rho_{\mathrm{f}}\, u_0\, d_{\mathrm{p}}}{\mu_{\mathrm{f}}} \qquad \text{Eq. A.12}$$

$$Sc = \frac{\mu_{\mathrm{f}}}{\rho_{\mathrm{f}}\, D_{\mathrm{m}}} \qquad \text{Eq. A.13}$$

- **Thermal conductivity of the gas ($\lambda_f$)**

$\lambda_f$ is determined in accordance with the Wassiljewa method[68] (Eq. A.14).

$$\lambda_{\mathrm{f}} = \sum_{i=1}^{n} \frac{y_i\, \lambda_i}{\sum_{j=1}^{n} (y_j\, A_{ij})} \qquad \text{Eq. A.14}$$

where $\lambda_i$ is thermal conductivity of species $i$, estimated following the Eucken method[66] (Eq. A.15).

$$\lambda_i = \mu_i \left(1.25\, \frac{R_{\mathrm{g}}}{M_i} + \frac{C_{\mathrm{p},i}}{M_i}\right) \qquad \text{Eq. A.15}$$

$A_{ij}$ is a dimensionless parameter based on Mason and Saxena method[68] for the mixture of species $i$ and $j$ (Eq. A.16).

$$A_{ij} = \frac{\left[1 + \left(\frac{\lambda_{\mathrm{tr},i}}{\lambda_{\mathrm{tr},j}}\right)^{1/2} + \left(\frac{M_i}{M_j}\right)^{1/4}\right]^2}{\left[8\left(1 + \frac{M_i}{M_j}\right)\right]^{0.5}} \qquad \text{Eq. A.16}$$

In turn, $\frac{\lambda_{\mathrm{tr},i}}{\lambda_{\mathrm{tr},j}}$ corresponds to the translational thermal conductivities and can be achieved from Eq. A.17[68].

$$\frac{\lambda_{\mathrm{tr},i}}{\lambda_{\mathrm{tr},j}} = \frac{\Gamma_j \left[exp\left(0.0464\ T_{r,i}\right) - exp\left(-0.2412\ T_{r,i}\right)\right]}{\Gamma_i \left[exp\left(0.0464\ T_{r,j}\right) - exp\left(-0.2412\ T_{r,j}\right)\right]} \qquad \text{Eq. A.17}$$

$T_{\mathrm{r},i}$ is the reduced temperature of species $i$ and it is equal to $T/T_{\mathrm{c},i}$.

$\Gamma_i$ (m·K·W$^{-1}$) is determined by Eq. A.18[68].

$$\Gamma_i = 210 \left(\frac{T_{\mathrm{c},i}\ {M_i}^3}{{P_{\mathrm{c},i}}^4}\right)^{1/6} \qquad \text{Eq. A.18}$$

- **Axial heat dispersion coefficient ($\lambda_{ax}$)**

$\lambda_{\mathrm{ax}}$ is calculated through the Wakao and Funazkri correlation[69](Eq. A.19).

$$\lambda_{\mathrm{ax}} = 7\ \lambda_{\mathrm{f}} + 0.5\ \rho_{\mathrm{f}}\ u_0\ d_{\mathrm{p}}\ C_{\mathrm{p,f}} \qquad \text{Eq. A.19}$$

- **Global coefficient for heat transfer ($U$)**

$U$ is determined by Eq. A.20.

$$\frac{1}{U} = \frac{1}{h^{\mathrm{int}}} + \frac{A^{\mathrm{int}}\ ln\left[\left(r^{\mathrm{int}} + \delta^{\mathrm{shell}}\right)/r^{\mathrm{int}}\right]}{2\ \pi\ L\ k^{\mathrm{shell}}} + \frac{A^{\mathrm{int}}}{A^{\mathrm{ext}}}\ \frac{1}{h^{\mathrm{out}}} \qquad \text{Eq. A.20}$$

where $h^{\mathrm{int}}$ is the convective heat transfer coefficient between the gaseous phase and the shell, $\delta^{\mathrm{shell}}$ represents the shell thickness, $k^{\mathrm{shell}}$ is the shell thermal conductivity and $h^{\mathrm{out}}$ stands for the convective transfer coefficient in the oven.

For $k^{\mathrm{shell}}$ it was used the typical value for stainless steel (14.4 W·m$^{-1}$·K$^{-1}$)[65] and for $h^{\mathrm{out}}$ it was considered the typical value for air natural convection (50 W·m$^{-2}$·K$^{-1}$)[65].

$h^{\mathrm{int}}$ is calculated by Eq. A.21 from Li-Finlayson:

$$h^{\mathrm{int}} = 0.17\ \frac{\lambda_{\mathrm{f}}}{d_{\mathrm{p}}}\ \left(\frac{Pr}{0.7}\right)^{1/3}\ Re^{0.79} \qquad \text{Eq. A.21}$$

where $\lambda_f$ is the thermal conductivity of the gas mixture, $d_p$ the catalyst particle diameter, $Re$ and $Pr$ are the Reynolds and Prandtl (Eq. A.22) dimensionless numbers, respectively.

$$Pr = \frac{\mu_{\mathrm{f}}\ C_{\mathrm{p,f}}}{\lambda_{\mathrm{f}}} \qquad \text{Eq. A.22}$$

## Notation:

$A^{\mathrm{ext}}$- external axial area of the reactor;

$A^{\mathrm{int}}$- internal axial area of the reactor;

$A_{ij}$ - dimensionless parameter;

$C_{\mathrm{p,f}}$ - Specific heat capacity of the gas mixture;

$C_{\mathrm{p},i}$ - molar heat capacity of species $i$;

$D_{\mathrm{ax}}$ - mass axial dispersion coefficient;

$D_{\mathrm{m,f}}$ - molecular diffusivity of the gas mixture;

$D_{\mathrm{m},i}$ - molecular diffusivity of species $i$;

$d_{\mathrm{p}}$ - catalyst particle diameter;

$h^{\mathrm{int}}$ - convective heat transfer coefficient between the gaseous phase and the shell;

$h^{\mathrm{out}}$ - convective transfer coefficient in the oven;

$k^{\mathrm{shell}}$ - shell thermal conductivity;

$M_i$ - molar weight of species $i$;

$P$ - total pressure;

$P_{\mathrm{c},i}$ - critical pressure for species $i$;

$Pe$ - Péclet number;

$Pr$ - Prandtl number;

$r^{\mathrm{int}}$ - internal reactor radius;

$Re$ - Reynolds number;

$R_{\mathrm{g}}$ - ideal gas constant;

$Sc$ - Schmidt number;

$T$ - temperature;

$T_{\mathrm{c},i}$ - critical temperature for species $i$;

$T_{\mathrm{r},i}$ - reduced temperature of species $i$;

$U$ - global coefficient for heat transfer;

$u_0$ - superficial velocity;

$y_i$ - molar fraction of species $i$;

$\delta^{\mathrm{shell}}$ - shell thickness;

$\lambda_{\mathrm{ax}}$ - axial heat dispersion coefficient;

$\lambda_{\mathrm{f}}$ - thermal conductivity of the gas mixture;

$\lambda_i$ - thermal conductivity of species $i$;

$\frac{\lambda_{\mathrm{tr},i}}{\lambda_{\mathrm{tr},j}}$ - translational thermal conductivities;

$\mu_{\mathrm{f}}$ - viscosity of the gas mixture;

$\mu_i$ - viscosity of species $i$;

$\rho_{\mathrm{f}}$ - density of the gas mixture;

$\phi_{ij}$ - binary term for the mixture of species $i$ and $j$;

$(\sum v)_i$ - sum of the atomic diffusion volumes for species $i$.

# Appendix B - Equations used to determine thermodynamic limit of $CO_2$ conversion

This appendix presents the reasoning followed for determining the thermodynamic limits based on the feed conditions.

- Inlet total molar flow rate ($F^0$)

$$F^0 = \frac{Q^0\ P^0}{R\ T^0} \qquad \text{Eq. B.1}$$

- Inlet molar flow rate of species $i$ ($F_i^0$)

$$F_i^0 = F^0\ y_i^0 \qquad \text{Eq. B.2}$$

- Molar flow rate of species $i$ ($F_i$) as a function of the conversion, $X_A$

$$F_i(X_A) = F_i^0 + \frac{\upsilon_i}{\upsilon_A}\ F_A^0\ X_A \qquad \text{Eq. B.3}$$

- Total molar flow rate ($F$) as a function of $X_\mathrm{A}$

$$F(X_A) = \sum_{i=1}^{j} F_i(X_A) \qquad \text{Eq. B.4}$$

- Total volumetric flow rate ($Q$) as a function of $X_A$

$$Q(X_\mathrm{A}) = \frac{Q^0\ F}{F^0} \qquad \text{Eq. B.5}$$

Deduction:

$$P\ Q = F\ R_g\ T \qquad \text{(B. 5.1)}$$

$$P^0\ Q^0 = F^0\ R_g\ T^0 \qquad \text{(B. 5.2)}$$

$$\frac{P\ Q}{P^0\ Q^0} = \frac{F\ R_g\ T}{F^0\ R_g\ T^0} \qquad \text{B. 5.3}$$

Assuming constant temperature and pressure:

$$Q = \frac{Q^0\ F}{F^0}$$

- Partial pressure of species $i$ as a function of $X_A$

$$p_i(X_A) = \frac{F_i\, R_g\, T}{Q} \qquad \text{Eq. B.6}$$

- Using Eq. B.7, it is obtained the equilibrium $X_A$ ($X_{A_{eq}}$) correspondent to the thermodynamic limit.

$$\Re(X_{A_{eq}}) = 0 \qquad \text{Eq. B.7}$$

## Notation:

$A$ – reference species ($CO_2$);

$F$ – total molar flow rate;

$F_i$ – molar flow rate of species $i$;

$F^0$ – inlet total molar flow rate;

$F_i^0$ – inlet molar flow rate of species $i$;

$j$ – number of species;

$P$ – total pressure;

$P^0$ – inlet pressure;

$p_i$ – partial pressure of species $i$;

$Q$ – total volumetric flow rate;

$Q^0$ – inlet total volumetric flow rate;

$R_g$ – ideal gas constant;

$T$ – temperature;

$T^0$ – inlet temperature;

$X_i$ – conversion of species $i$;

$X_{i_{eq}}$ – equilibrium conversion of species $i$;

$\Re$ – reaction rate;

$v_i$ – Stoichiometric coefficient of species $i$ (<0 for reaction reagents; >0 for reaction products);

# Appendix C – Detailed information and respective fitting parameters used to represent the model predicted adsorption equilibrium isotherms in section 4.5.3

Detailed information and respective fitting parameters used to represent the model predicted adsorption equilibrium isotherms for all the species considered in section 4.5.3 are presented below.

- **Freundlich model for $H_2O$ adsorption equilibrium on 4A BFK at 100 ºC**

Table C.1 – Fitting parameters of Freundlich adsorption isotherm for water on zeolite 4A BFK at 100 ºC.

| Parameter | Value | $t_{stat}$ | $p-Value$ |
|---|---|---|---|
| $K_F$ (mol·kg$^{-1}$·Pa$^{-1/n}$) | 1.657 ± 0.127 | 13.00 | $9.542 \times 10^{-15}$ |
| $1/n$ | 0.2305 ± 0.0102 | 22.58 | $4.784 \times 10^{-22}$ |

$K_F$ is the Freundlich adsorption constant and $n$ is a dimensionless empirical constant. $t_{stat}$ and $p-value$ are statistical parameters that assess the significance of the results.

- **Freundlich model for $H_2O$ adsorption equilibrium on 13X BFK at 100 ºC**[62]

Table C.2 – Fitting parameters of Freundlich adsorption isotherm for water on zeolite 13X BFK at 100 ºC.

| Parameter | Value | $t_{stat}$ | $p-Value$ |
|---|---|---|---|
| $K_F$ (mol·kg$^{-1}$·Pa$^{-1/n}$) | 2.577 ± 0.136 | 18.92 | $2.651 \times 10^{-10}$ |
| $1/n$ | 0.2039 ± 0.0072 | 28.30 | $2.354 \times 10^{-12}$ |

$K_F$ is the Freundlich adsorption constant and $n$ is a dimensionless empirical constant. $t_{stat}$ and $p-value$ are statistical parameters that assess the significance of the results.

- **Langmuir model for $CO_2$, $CH_4$ and $N_2$ adsorption equilibrium on 4A BFK**[48]

To determine adsorption equilibrium isotherm of $CH_4$ and $N_2$, Eq. C.1 (Langmuir) should be used, while for $CO_2$ Eq. C.2 (dual-site Langmuir) should be considered instead.

$$q_i = q_{\max,i}\,\frac{K_i\,p}{1+K_i\,p} \qquad \text{Eq. C.1}$$

$$q_i = q_{\max1,i}\,\frac{K_{1,i}\,p}{1+K_{1,i}\,p} + q_{\max2,i}\,\frac{K_{2,i}\,p}{1+K_{2,i}\,p} \qquad \text{Eq. C.2}$$

$$K_{\mathrm{L},i} = K_i^0\,\exp\left(-\frac{\Delta H}{R_\mathrm{g}\,T}\right) \qquad \text{Eq. C.3}$$

where: $q_i$ is the adsorbed amount of species $i$; $q_{\max,i}$ is the maximum adsorption capacity of species $i$ in the adsorbent; $K_{\mathrm{L},i}$ is the Langmuir adsorption constant for species $i$; $K_i^0$ is the pre-exponential factor of adsorption constant; $R_\mathrm{g}$ is the ideal gas constant; $(-\Delta H)$ is the heat of adsorption; $T$ is the temperature and $p$ is the partial pressure.

Table C.3 - Fitting parameters of the Langmuir model for $CO_2$, $CH_4$ and $N_2$ adsorption equilibrium on 4A BFK.

| **Species** | $\boldsymbol{q_{\max,i}}$ (mol·kg$^{-1}$) | | $\boldsymbol{K_i^0}$ (bar$^{-1}$) | | $(-\Delta \boldsymbol{H})$ (kJ·mol$^{-1}$) | |
|---|---|---|---|---|---|---|
| **$CO_2$** | $\boldsymbol{q_{\max1,i}}$ | $\boldsymbol{q_{\max2,i}}$ | $\boldsymbol{K_{1,i}^0}$ | $\boldsymbol{K_{2,i}^0}$ | $(-\Delta \boldsymbol{H})_1$ | $(-\Delta \boldsymbol{H})_2$ |
| | 1.81 | 3.68 | $2.01\times 10^{-8}$ | $1.76\times 10^{-5}$ | 42.3 | 36.6 |
| **$CH_4$** | 3.47 | | $5.88 \times 10^{-5}$ | | 20.5 | |
| **$N_2$** | 3.24 | | $3.98 \times 10^{-5}$ | | 19.7 | |

- **Langmuir-Freundlich model for $CO_2$ and $CH_4$ adsorption equilibrium on 13X BFK at 100 ºC**[61]

$$q_i = \frac{q_{\max,i}\,K_\mathrm{LF}\,p^n}{1+K_\mathrm{LF}\,p^{\,n}} \qquad \text{Eq. C.4}$$

where $q_i$ is the adsorbed amount of species $i$, $q_{\max,i}$ is the maximum adsorption capacity of species $i$ in the adsorbent, $p$ is the partial pressure and $K_\mathrm{LF}$ is the Langmuir-Freundlich adsorption constant for species $i$.

Table C.4 - Fitting parameters of the Langmuir-Freundlich model for $CO_2$, $CH_4$ and $N_2$ adsorption equilibrium on 13X BFK at 100 ºC.

| Species | $q_{max}$ (mol·kg$^{-1}$) | $K_{LF}$ (mol·kg$^{-1}$·bar$^{-1/n}$) | $n$ | $Se$ |
|---|---|---|---|---|
| **$CO_2$** | 6.705 ± 0.056 | 0.8124 ± 0.0158 | 0.7421 ± 0.0207 | $1.395 \times 10^{-3}$ |
| **$CH_4$** | 4.020 ± 0.238 | $(3.154 \pm 0.808) \times 10^{-2}$ | 1.222 ±0.124 | $7.864 \times 10^{-3}$ |

$Se$ measures the variance of the obtained results and is obtained by Eq. C.5.

$$Se = \frac{\sum_{j=1}^{n_{exp}} (q_{\mathrm{exp},i} - q_{\mathrm{mod},i})^2}{(n_{\mathrm{exp}} - a)} \qquad \text{Eq. C.5}$$

where $q_{\mathrm{exp},i}$ stands for the experimental value of adsorbed amount of species $i$, $q_{\mathrm{mod},i}$ is the corresponding model value, $n_{\mathrm{exp}}$ corresponds to the total number of experimental points and $a$ is the number of parameters in the model.

## Notation:

$a$ - number of parameters in the model;

$K_{\mathrm{F}}$ - Freundlich adsorption constant;

$K_i^0$ – pre-exponential factor of adsorption constant;

$K_{\mathrm{LF}}$ - Langmuir-Freundlich adsorption constant for species $i$;

$K_{\mathrm{L},i}$ - Langmuir adsorption constant for species $i$;

$n$ is a dimensionless empirical constant;

$n_{\mathrm{exp}}$ - total number of experimental points;

$p$ – partial pressure;

$q_{\mathrm{exp},i}$ - experimental value of adsorbed amount of species $i$;

$q_i$ - adsorbed amount of species $i$;

$q_{\mathrm{max},i}$ maximum adsorption capacity of species $i$ in the adsorbent;

$q_{\mathrm{mod},i}$ - model value of adsorbed amount of species $i$;

$R_{\mathrm{g}}$ – ideal gas constant;

$T$ – temperature;

$\Delta H$ - heat of adsorption.